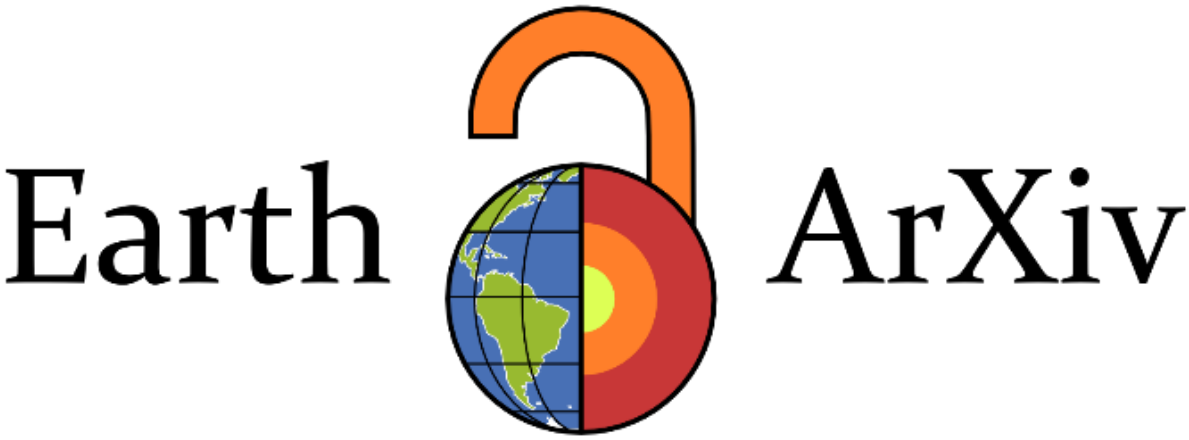

# Warm deep ocean temperatures from clumped isotopes suggest high climate sensitivity in early Cenozoic hothouse

**Authors:**

Tobias Agterhuis[1,a*], Martin Ziegler[1], Brendan Oerlemans[1,b], Sai Ke[1,c], Bastiaan L. P. Koene[1], Lea de Vries[1,d], Meya Kersten[1], Sanne Posthuma[1], Anne Roozendaal[1] & Lucas J. Lourens[1]

**Affiliations:**

[1]Department of Earth Sciences, Faculty of Geosciences, Utrecht University, Utrecht, the Netherlands

[a]Now at: School of Ocean and Earth Science, National Oceanography Centre Southampton, University of Southampton, Southampton, United Kingdom

[b]Now at: Department of Earth Sciences, Faculty of Science, Vrije Universiteit Amsterdam, Amsterdam, the Netherlands

[c]Now at: Sorbonne Université, CNRS, EPHE, PSL, UMR METIS, Paris, France

[d]Now at: Aeres University of Applied Sciences, Almere, the Netherlands

*Corresponding author. Email: t.agterhuis@soton.ac.uk

**Abstract**

The early Cenozoic was characterized by the warmest climates and highest atmospheric $CO_2$ levels of the past 85 Myrs. Reconstructions of deep ocean temperatures based on benthic foraminiferal oxygen isotope records are typically used to infer Earth's global climate state during this hothouse world. However, this approach requires uncertain assumptions, regarding the seawater isotope composition and pH, and species-specific vital effects. Here we use clumped isotope thermometry, a proxy not complicated by non-thermal influences, to reconstruct early Cenozoic deep ocean temperatures on million-year time scales from the South Atlantic Ocean. We find on average warmer temperatures than previously derived from oxygen isotopes, consistent with clumped isotope reconstructions from the North Atlantic. These results challenge our understanding of seawater isotope composition in an ice-free world and invoke potential pH effects on the benthic oxygen isotopes. Deep ocean temperatures reached maximum values of up to 20 °C during the Early Eocene Climatic Optimum, which is >5 °C warmer than previously thought. These findings imply that (past) climate sensitivity to pCO2 forcing was much higher (6 to 8 °C) than currently used in climate models that simulate future warming scenarios of the IPCC (2.5 to 4.0 °C).

## Introduction

The ocean is responsible for most of the heat transport from the equator to the polar latitudes and is an important

reservoir of carbon available in the climate system (Trenberth & Caron, 2001; Rose & Ferreira, 2013). Changes in the strength and patterns of ocean circulation influence the heat distribution and ocean carbon storage capacity (Anderson et al., 2009; Srokosz et al., 2012). The deep ocean is therefore considered to represent a key factor in regulating the state and evolution of Earth's global climate and the global carbon cycle through time (Clark et al., 2002; Anderson et al., 2009; Sexton et al., 2011; Burke & Robinson, 2012; Kostov et al., 2014). Reconstruction of deep ocean temperatures, or basically bottom water temperatures (BWT), is hence essential to investigate climate states in the geological past. A time when ocean temperature conditions were fundamentally different from today is the early Cenozoic, and particularly the late Paleocene to early Eocene (59–48 Ma). Proxy reconstructions show that this period experienced the warmest climates of the Cenozoic associated with highly elevated atmospheric $CO_2$ levels (~800–2500 ppm) (Penman et al., 2014; Anagnostou et al., 2016, 2020; Gutjahr et al., 2017; Harper et al., 2020; Rae et al., 2021; CenCO2PIP, 2023) with no continental ice sheets on both hemispheres and a strongly reduced equator to pole surface temperature gradient (Tripati et al., 2003; Sluijs et al., 2006, 2009, 2011; Pearson et al., 2007; Zachos et al., 2008; Bijl et al., 2009, 2013; Hollis et al., 2012, 2019; Frieling et al., 2014, 2018; Inglis et al., 2015; Cramwinckel et al., 2018; Evans et al., 2018a; Harper et al., 2018; Gaskell et al., 2022; Fokkema et al., 2024a; Fokkema et al., 2024b; Kegel, Fokkema et al., 2025). Hence, the early Cenozoic is considered the most recent analogue for experiencing scenarios of high future $CO_2$ concentrations and associated global warming. Temperature reconstructions of this time may therefore provide important constraints on the sensitivity of the Earth's climate to elevated $CO_2$ levels (Burke et al., 2018; Inglis et al., 2020). In addition, these temperature estimates can be used to assess the performance of climate model simulations (Lunt et al., 2021).

Over the past three decades, records of oxygen isotopes (Zachos et al., 2001, 2008; McCarren et al., 2008; Stap et al., 2010; Littler et al., 2014; Lauretano et al., 2015, 2016, 2018; Barnet al., 2019; Thomas et al., 2018; Westerhold et al., 2018, 2020) and Mg/Ca ratios (Lear et al., 2000, 2010, 2015; Tripati & Elderfield, 2005; Cramer et al., 2011) obtained from the fossil shells of benthic foraminifera have been widely used to estimate BWT across the Cenozoic. Since recent years, measurements of clumped isotopes (or "multiply substituted isotopologues") have emerged as a new tool to reconstruct ocean temperatures (Rodríguez-Sanz et al., 2017; Evans et al., 2018a; Leutert et al., 2019, 2020, 2021; Modestou et al., 2020; Agterhuis et al., 2022; Meckler et al., 2022; Braaten et al., 2023; Hou et al., 2023; Taylor et al., 2023; Kocken et al., 2024). Carbonate clumped isotope thermometry ($\Delta_{47}$) builds on the temperature dependent abundance of bonds between the heavy carbon and heavy oxygen isotopes ($^{13}C$–$^{18}O$) within carbonate ions, with more "clumping" of these rare heavier isotopes occurring at lower temperatures (Gosh et al., 2006; Schauble et al., 2006; Eiler et al., 2007, 2011; Huntington & Petersen, 2023). Analytical advances over the past decade have significantly reduced sample size requirements and have enabled the reproducibility of measurements across different laboratories (Huntington et al., 2009; Schmid & Bernasconi, 2010; Dennis et al., 2011; He et al., 2012; Bernasconi et al., 2013, 2018, 2021; Hu et al., 2014; Meckler et al., 2014; Müller et al., 2017).

Importantly, unlike the traditional $\delta^{18}O$ and Mg/Ca proxies, clumped isotopes have the advantage that they are not affected by factors other than temperature. This clumping is independent of the isotope composition of the source water (Gosh et al., 2006; Schauble et al., 2006; Eiler et al., 2007, 2011; Huntington & Petersen, 2023). Several studies have furthermore shown that species-specific physiological differences (vital effects) in clumped isotope fractionation in foraminifera are small or non-existent (Tripati et al., 2010; Grauel et al., 2013; Breitenbach et al., 2018; Peral et al., 2018, 2022; Piasecki et al., 2019; Meinicke et al., 2020) and experiments and models have not found significant pH effects on $\Delta_{47}$ (Hill et al., 2014; Tang et al., 2014; Tripati et al., 2015; Kelson et al., 2017; Watkins & Hunt, 2015; Guo et al., 2020; Watkins & Devriendt, 2022).

Recently, the first clumped isotopes analysis on benthic foraminifera from Newfoundland, North Atlantic has revealed a new picture of BWT evolution across the early Cenozoic, with on average warmer temperatures than estimated from benthic oxygen isotopes ($\delta^{18}O_b$), as well as surprisingly large temperature fluctuations on what seem to be million-year time scales (Meckler et al., 2022). However, the reported temperature variations might to some extent represent a regional signal unique to the small North Atlantic basin instead of global BWT changes. To answer this question, here we present and discuss a late Paleocene-early Eocene $\Delta_{47}$-based BWT record of the South Atlantic, a region that constitutes a major part of Cenozoic $\delta^{18}O_b$ compilations (Cramer et al., 2011; Westerhold et al., 2020). For this purpose, we measured paired stable ($\delta^{18}O_b$ and $\delta^{13}C_b$) and clumped ($\Delta_{47}$) isotopes on several benthic foraminiferal species from ODP (Ocean Drilling Program) Sites 1262 and 1263 (Walvis Ridge) (Zachos et al., 2004, 2005) to produce multiple new BWT bins in the period 60–48 Ma (see Supplementary Figure S1 for paleogeographic map). Each of these individual temperature bins represent the background climate states (thereby excluding hyperthermal events) and are based on numerous replicate $\Delta_{47}$ measurements obtained from neighbouring samples, thereby each reflecting average conditions of 100–200 kyr intervals (see Methods).

From clumped isotopes, we find similarly warm BWT in the South Atlantic compared to the North Atlantic (Meckler et al., 2022). However, temperatures appear more stable than in the North Atlantic, suggesting that the deep South Atlantic captures more of a global signal. These warmer BWT from $\Delta_{47}$ than previously inferred from $\delta^{18}O_b$ challenge longstanding assumptions on the oxygen isotope composition of the seawater ($\delta^{18}O_{sw}$) in the early Cenozoic ice-free climate state. Potential pH effects on $\delta^{18}O_b$ are required to explain the temperature discrepancy between the two proxies. Clumped isotopes show a major warming in the entire deep Atlantic at the onset of Early Eocene Climatic Optimum (~52 Ma), which is accompanied by elevated atmospheric $CO_2$ levels. These higher BWT estimates from clumped isotopes suggest higher climate sensitivity to $pCO_2$ forcing across the early Cenozoic than previously appreciated.

**Results and Discussion**

**Deep ocean temperatures**

Our new $\Delta_{47}$-based BWT from the South Atlantic are, like those from the North Atlantic (Meckler et al., 2022), overall warmer than the temperatures calculated from $\delta^{18}O_b$ compiled for the South Atlantic (McCarren et al., 2008; Stap et al., 2010; Littler et al., 2014; Lauretano et al., 2015, 2016, 2018; Barnet al., 2019; Thomas et al., 2018; Westerhold et al., 2020) (Figure 1). The North Atlantic $\Delta_{47}$-data follows the new age model for IODP Site U1409 (Kirtland Turner et al., 2024), which changes the age of some data points up to 0.5 Myr compared to the original publication (Meckler et al., 2022). One might consider potential post depositional alteration of the $\Delta_{47}$ signal as cause for the temperature discrepancy with the oxygen isotopes. However, previous studies comparing sites with different sedimentation rates have not found a relationship between $\Delta_{47}$-based temperatures and burial depth, which challenges this explanation (Meckler et al., 2022). The high-resolution composite $\delta^{18}O_b$ record suggests that a gradual warming trend started from the late Paleocene onwards that culminated in a sustained period of peak global warmth, known as the EECO (~52–50 Ma) (Figure 1) (Westerhold et al., 2020). The clumped isotopes do not indicate a clear warming trend from the Paleocene into the early Eocene, though they reveal the warmest BWT at the EECO reaching up to exceptional values of ~20 °C. After this peak warmth, both the $\Delta_{47}$ and $\delta^{18}O_b$ data show a long-term cooling for the remainder of the Eocene. In comparison to the North Atlantic, our South Atlantic BWTs show less large amplitude variations and are on average cooler in the late Paleocene (~18 °C vs. 14 °C) and warmer in the early Eocene (~11 °C vs. 15 °C). These differences might point to periodically local sources of deep water in the North Atlantic (Hohbein et al., 2012; Cramwinckel et al., 2020; Vickers et al., 2020), while the South Atlantic and Pacific were bathed by water masses primarily formed in the southern high latitudes (Thomas et al., 2003, 2014; Via & Thomas, 2006; Huck et al., 2017; Batenburg et al., 2018; Zhang et al., 2020, 2022).

Early Cenozoic BWT derived from Mg/Ca appear to be different from both oxygen and clumped isotope reconstructions (Figure 1). In the Eocene, our $\Delta_{47}$-based BWT are both warmer than inferred from Mg/Ca and $\delta^{18}O_b$. The major warming during the EECO also does not appear in the Mg/Ca record. The $\Delta_{47}$ and Mg/Ca-based temperatures seem to be more consistent to each other in the Paleocene, being both warmer than estimated from $\delta^{18}O_b$. Unlike the $\delta^{18}O_b$ record, the Mg/Ca-based BWTs do not exhibit a warming trend towards the early Eocene. In fact, the warmest Mg/Ca-based temperatures occur in the Paleocene and show a long-term cooling trend afterwards. In addition, there is high variability and 1–4 Myr oscillations in the Mg/Ca data that are not observed in the $\delta^{18}O_b$ record (the clumped isotope record being of too low resolution to make a comparison). However, the longer-term oscillations are probably an artifact because of aliasing higher frequency variability (Cramer et al., 2011). Like oxygen isotopes, foraminiferal Mg/Ca is also affected by seawater chemistry. Reconstructions of BWT before 48 Ma have been considered to be unreliable (Miller et al., 2020) because of large uncertainties in the Mg/Ca composition of the past seawater (Lowenstein et al., 2001; Horita et al., 2002; Coggon

et al., 2010; Broecker & Yu, 2011; Evans & Müller, 2012; Lear et al., 2015; Evans et al., 2016; Evans et al., 2018b) This might explain the apparent cooling trend in the early Cenozoic Mg/Ca-based BWT. In addition, other non-thermal influences that complicate the Mg/Ca proxy might play a role, such as the carbonate saturation state (Elderfield et al., 2006; Yu & Elderfield, 2008; Lear et al., 2010; Kender et al., 2014; Evans et al., 2018b; Gray et al., 2018), and vital effects (Lear et al., 2002; Marchitto et al., 2007).

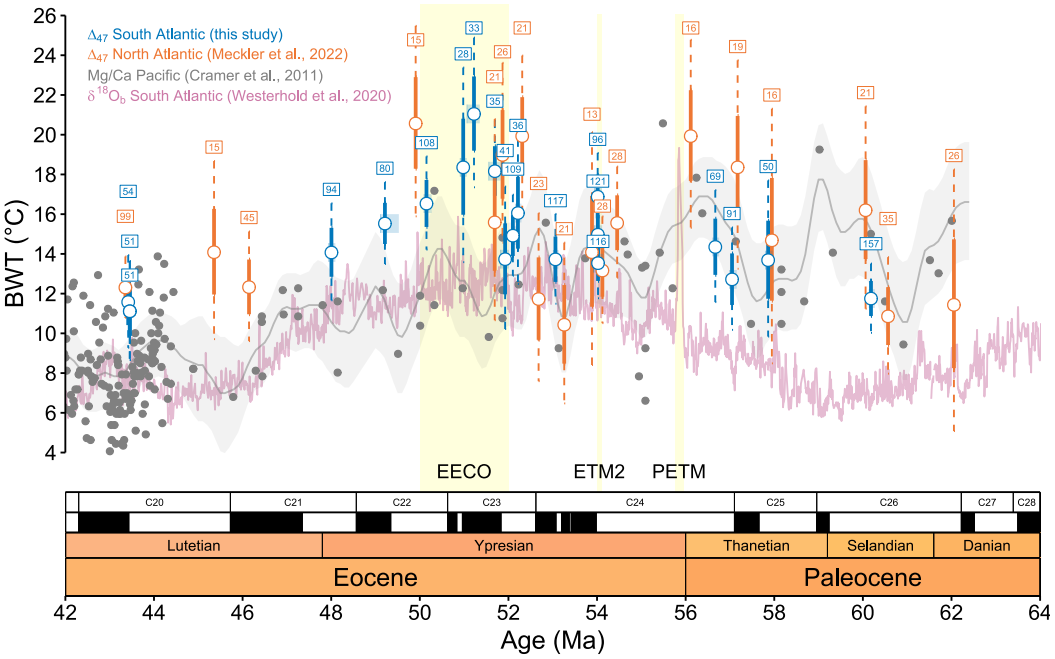


**Figure 1.** Comparison of early Cenozoic BWTs based on $\delta^{18}O_b$ from the Walvis Ridge, South Atlantic (ODP Sites 1262/1263/1265) (McCarren et al., 2008; Stap et al., 2010; Littler et al., 2014; Lauretano et al., 2015, 2016, 2018; Thomas et al., 2018; Barnet al., 2019; Westerhold et al., 2020), Mg/Ca with trend and shaded 90% confidence intervals from Cramer et al., 2011 calibrated following Lear et al., 2010, and $\Delta_{47}$ from the Walvis Ridge, South Atlantic (ODP Sites 1262/1263) (this study; Leutert et al., 2019; Agterhuis et al., 2022) and Newfoundland, North Atlantic (IODP Sites U1407/U1409) (Leutert et al., 2019; Meckler et al., 2022). The Mg/Ca-based temperatures are primarily derived from Shatsky Rise, Western Pacific (ODP Site 1209) (Dutton et al., 2005a, 2005b) with additional data around ~55 Ma from the Weddell Sea, Southern Ocean (ODP Site 689) (Lear et al., 2000; Billups & Schrag, 2003). The two South Atlantic clumped isotope temperature bins (n = 28 and n = 33) in the middle part of the EECO originate from a single bin published in Meckler et al., 2022, which was separated into two parts in our study because of the relatively long duration of the bin. The North Atlantic $\Delta_{47}$ data is plotted following the new age model for IODP Site U1409 (Kirtland Turner et al., 2024). The error bars on the $\Delta_{47}$-based temperatures indicate 68% (solid) and 95% (dashed) confidence intervals, representing fully propagated analytical and calibration uncertainties. Numbers above $\Delta_{47}$ data bins represent the number of (replicate) measurements. The $\Delta_{47}$-derived temperatures were calculated using the foraminiferal clumped isotope calibration by Meinicke et al., 2020, 2021 (see Methods). The effect of using an alternative clumped isotope calibration on the temperature estimates is shown in Supplementary Figure S5. The $\delta^{18}O_b$ data were corrected to *Cibicidoides* values (seawater equilibrium) before calculation of BTW using the calibration of Marchitto et al., 2014 (see Methods). The record represents a 5 pts LOESS smoothing of data averaged in 5 kyr time steps.

**Oxygen isotope composition of the seawater**

A major implication of the warmer BWT derived from clumped isotopes in comparison to $\delta^{18}O_b$ is that they suggest that longstanding assumptions on the $\delta^{18}O_{sw}$ in the early Cenozoic hothouse are not valid and require a re-assessment. Benthic oxygen isotope records represent a combined signal of BWT and $\delta^{18}O_{sw}$ (Ravelo & Hillaire-Marcel, 2007; Pearson, 2012; Raymo et al., 2018). For the early Cenozoic, a constant $\delta^{18}O_{sw}$ value of –1‰ based on the absence of ice sheets is commonly used in the calculation of $\delta^{18}O_b$-derived BWT (Shackleton, 1986). Seawater isotope composition can be calculated when we combine the clumped isotope-derived temperatures with the oxygen isotope data of our measurements (see Methods). Our simultaneously obtained $\delta^{18}O_b$ and $\delta^{13}C_b$ data are consistent with previous studies (Supplementary Figure S2) (Littler et al., 2014; Lauretano et al., 2015, 2016, 2018; Westerhold et al., 2020).

We find that the inferred $\delta^{18}O_{sw}$ is much higher than the assumed composition based on an ice-free world (Figure 2a). A first explanation would be that large ice sheets like present-day existed in the Paleocene and Eocene, which however seems highly unlikely given the evidence for subtropical temperatures and fossil evidence of palm trees and crocodiles in the polar regions (Sluijs et al., 2006, 2009; Bijl et al., 2009; Pross et al., 2012). Furthermore, records of ice-rafted debris only support the existence of small ice caps starting in the middle Eocene on Antarctica (Carter et al., 2017; Gulick et al., 2017; Barr et al., 2022) and the northern high-latitudes (Eldrett et al., 2007; St. John, 2008; Stickley et al., 2009; Darby, 2014; Tripati & Darby, 2018; Spray et al., 2019), only eventually culminating millions later in large-scale Antarctic glaciation at the Eocene-Oligocene Transition (Ehrmann & Mackensen, 1992; Zachos et al., 1992; Scher et al., 2011; Galeotti et al., 2016; Passchier et al., 2017; Klages et al., 2024). Other factors have been proposed to influence the $\delta^{18}O_{sw}$ on a global scale, such as isotope exchange between seawater and ocean crust at mid-ocean ridges, and ground water storage on land. Changes in mid-ocean ridge spreading rates may be able to influence the seawater isotope budget on multi-million-year timescales (Wallmann, 2001; Jaffrés et al., 2007), however, the global rates in the early Cenozoic were not different from today (Conrad & Lithgow-Bertelloni, 2007; Müller et al., 2008). Discharging and charging of continental aquifers has been invoked to explain large fluctuations in reconstructed sea level in the Cretaceous hothouse climate (Sames et al., 2020), however direct evidence for this is not available (Davies et al., 2020). Changes in deep ocean salinity is another factor that can alter $\delta^{18}O_{sw}$, but only on local/regional scales as the global ocean water isotope budget is constant (Ravelo & Hillaire-Marcel, 2007; Pearson, 2012). Deep ocean salinity reflects the evaporation-precipitation regime in the source regions of the deep water (Ravelo & Hillaire-Marcel, 2007; Pearson, 2012), and changes in $\delta^{18}O_{sw}$ could therefore indicate shifts in the distribution of different water masses (changes in ocean overturning circulation) (Meckler et al., 2022).

**pH effects on the oxygen isotopes**

Alternatively, instead of an underestimation of $\delta^{18}O_{sw}$, it could be that we are observing an effect of lower ocean pH on the incorporation of the oxygen isotopes in the foraminiferal tests (Spero et al., 1997; Uchikawa & Zeebe, 2010). Theory predicts this pH ($CO_3^{2-}$) effect, suggesting that the oxygen isotope values of foraminifera should become higher with decreasing pH with a slope of −1.42 ‰/unit pH (Zeebe, 1999, 2001) based on results from inorganic calcite precipitation experiments (McCrea, 1950; Usdowski & Hoefs, 1993). Oxygen isotope-based temperatures are calculated using calibrations established at modern ocean pH (e.g, Marchitto et al., 2014). Low-resolution reconstructions based on boron isotopes indicate that deep ocean was more acidic in the early Cenozoic, with pH on average about 0.5 units lower than present-day (pH of ~7.5 vs. ~8.0, respectively) (Lauvset et al., 2020; Meckler et al., 2022) (Figure 2b), which can be attributed to the elevated atmospheric $CO_2$ levels (Figure 2c). If not corrected for this lower pH, elevated foraminiferal $\delta^{18}O$ values would be interpreted as apparent cooler temperatures. Note that there is only direct evidence for a pH effect on the oxygen isotopes of planktic foraminifera from culture experiments, which show different slopes for this effect between species (Spero et al., 1997). At present, it is unclear from sediment core top studies whether this effect also exists for benthic foraminifera (Rathmann & Kuhnert, 2008; Marchitto et al., 2014). Nonetheless, if we correct the $\delta^{18}O_b$ measurements for a pH effect (using the theoretical slope of 1.42 ‰/unit pH), it brings the reconstructed $\delta^{18}O_{sw}$ closer to the assumed –1‰ value (Figure 2a). Thus, a large part of the BWT mismatch (approximately 2 to 3°C) between the clumped- and oxygen isotopes might be explained by a so far neglected pH effect on the $\delta^{18}O_b$ (Meckler et al., 2022; Evans et al., 2024; Rohling et al., 2024). Changes in the salinity of the deep water might then explain the residual variability in $\delta^{18}O_{sw}$, or there are changes in deep ocean pH that are not captured in the low-resolution deep ocean pH reconstruction used for our corrections (Fig. 2b).

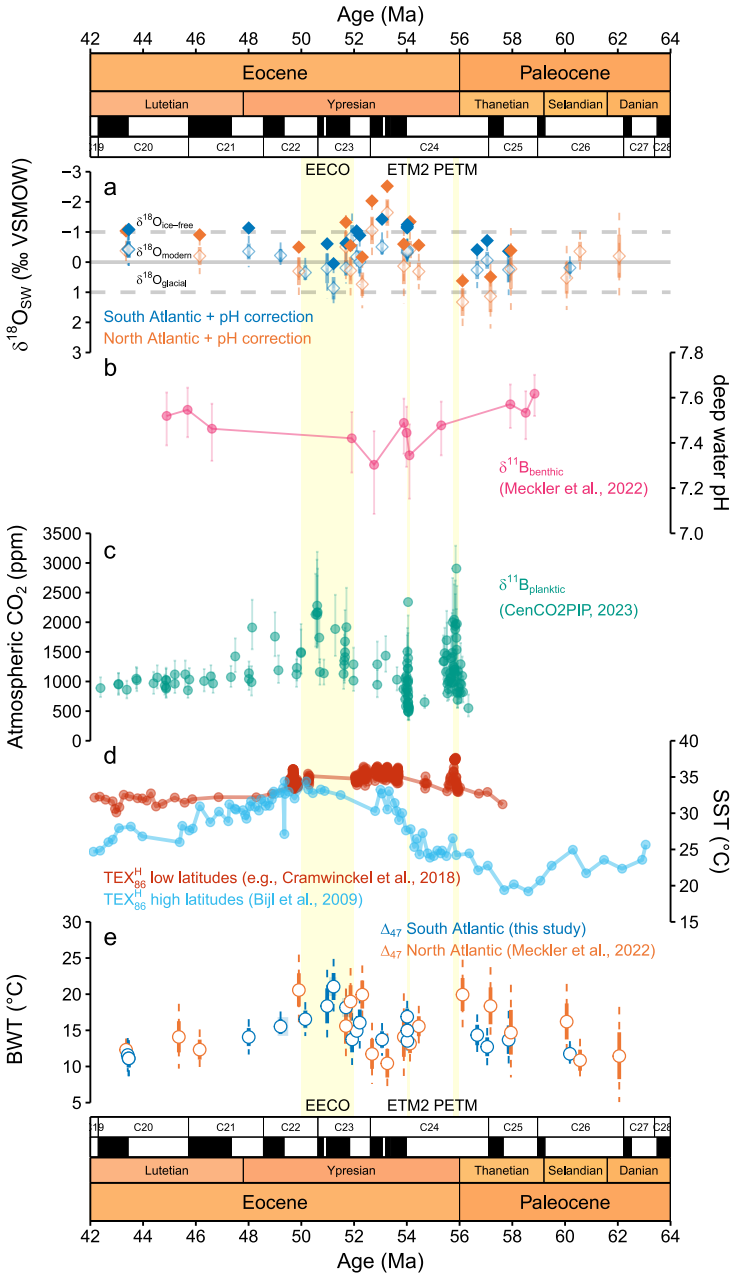


**Figure 2. a)** inferred $\delta^{18}O_{sw}$ composition from the combined $\Delta_{47}$-based BWT and $\delta^{18}O_b$ data (corrected to *Cibicidoides* values) from the Walvis Ridge, South Atlantic (ODP Sites 1262/1263) (this study; Leutert et al., 2019; Agterhuis et al., 2022) and Newfoundland, North Atlantic (IODP Sites U1407/U1409) (Leutert et al., 2019; Meckler et al., 2022) (see Methods). The data represented with a closed fill indicate the $\delta^{18}O_{sw}$ values corrected for an assumed pH effect on the $\delta^{18}O_b$. **b)** deep water pH based on boron isotopes of benthic foraminifera from the North Atlantic (ODP Sites 1258/1260 and IODP Site U1409) (Meckler et al., 2022). **c)** atmospheric $CO_2$ level reconstructions based on boron isotopes on planktic foraminifera (Penman et al., 2014; Anagnostou et al., 2016, 2020; Gutjahr et al., 2017; Harper et al., 2020; Rae et al., 2021; CenCO2PIP, 2023). **d)** sea surface temperature reconstructions based on $TEX_{86}$ from the equatorial Atlantic (ODP Site 959) (Cramwinckel et al., 2018; Frieling et al., 2018; Fokkema et al., 2024a; Kegel, Fokkema et al., 2025) and the Southern Ocean (ODP Site 1172) (Bijl et al., 2009). **e)** $\Delta_{47}$-based BWTs from the Walvis Ridge, South Atlantic (ODP Sites 1262/1263) (this study; Leutert et al., 2019; Agterhuis et al., 2022) and Newfoundland, North Atlantic (IODP Sites U1407/U1409) (Leutert et al., 2019; Meckler et al., 2022).

**High climate sensitivity**

At the start of the EECO around 52 Ma, a major warming (~5 °C) is recorded in the deep Atlantic, reaching exceptional peak temperatures of up to ~20 °C (Figures 1 and 2e). This rise in BWT coincides with elevated atmospheric $CO_2$ levels up to ~2000 ppm, as reconstructed from boron isotopes (Figure 2c), which approach peak-PETM values (Penman et al., 2014; Anagnostou et al., 2016, 2020; Gutjahr et al., 2017; Harper et al., 2020; Rae et al., 2021; CenCO2PIP, 2023). This co-occurrence could suggest a global $pCO_2$ forcing of these very warm temperatures, implying a rise in global temperatures. This warming seems however absent in current sea surface temperature reconstructions (Figure 2d) (Tripati et al., 2003; Bijl et al., 2009, 2013; Frieling et al., 2014; Inglis et al., 2015; Cramwinckel et al., 2018; Fokkema et al., 2024a), which might be because of a geographical bias (Judd et al., 2020). The rise in $CO_2$ levels during the EECO may be related to an increase in volcanic activity in several igneous provinces (Storey et al., 2007; Lee et al., 2013; Reagan et al., 2013; Brune et al., 2017; Zhang et al., 2023), decreased marine primary productivity (weaker biological pump) (Hilting et al., 2008), and/or ventilation of dissolved inorganic carbon as proposed for the short-lived early Eocene hyperthermal events (Sexton et al., 2011). Interestingly, the onset of highly elevated BWT occurs before a global positive shift in carbon isotope records (Zachos et al., 2010; Kirtland Turner et al., 2014; Lauretano et al., 2016, 2018; Westerhold et al., 2018) (Supplementary Figure S2), suggesting that the warming may indirectly have affected the global carbon cycle.

For a long time now, BWT have intuitively been used to track the evolution of the global climate state over the Cenozoic, as the deep ocean constitutes the largest heat reservoir and represents a relatively stable component in the climate system (Zachos et al., 2001; Hansen et al., 2013; Westerhold et al., 2020). Recently, two studies that analysed climate simulation results from an ensemble of models have shown that BWT changes correlate with global mean surface temperature (GMST) changes in an approximate 1:1 ratio (Goudsmit-Harzevoort et al., 2023; Evans et al., 2024), consistent with early arguments by Hansen et al, 2013. In other words, the global average BWT change equals the global surface temperature change. Thus, a peak BWT of ~19 °C during the EECO would translate to a GMST of ~33 °C (considering modern BWT of ~0 °C and GMST of ~14 °C) (Goudsmit-Hazevoort et al., 2023; Evans et al., 2024). Such highly elevated GMST is also found for the Paleocene-Eocene Thermal Maximum (PETM; 56 Ma) based on sea surface temperature reconstructions (Tierney et al., 2022). Our new South Atlantic BWT estimates from clumped isotopes can be placed into a broader perspective of global climate. For this, we need to assume that the reconstructed South Atlantic BWT are representative for the global deep ocean, i.e., a homogeneous global deep ocean. While awaiting clumped isotope early Cenozoic BWT reconstructions from the Pacific, small interbasinal isotopic differences ($\delta^{13}C_b$ and $\delta^{18}O_b$) found between the South Atlantic and Pacific during this time support this assumption (Cramer et al., 2009; Lauretano et al., 2018; Westerhold et al., 2018). Clumped isotope records from the Pacific are available for the Eocene-Oligocene Transitions (~34 Ma) and show BWT of

~11 °C during the latest Eocene (Taylor et al., 2023), which are very similar to $\Delta_{47}$-based Atlantic BWT reconstructions for a time slice in the middle Eocene (~43 Ma) (Leutert et al., 2019). In addition, climate model simulations of the early Eocene also show little variation in BWT (typically <1°C) around the globe (Goudsmit-Harzevoort et al., 2023).

Using our new BWT in conjunction with atmospheric $CO_2$ level reconstructions allows for the opportunity to reassess climate sensitivity through the Cenozoic. The most used form of climate sensitivity in future climate projections is Equilibrium Climate Sensitivity, defined as the equilibrium GMST increase in response to a doubling in atmospheric $CO_2$ levels (PALAEOSENS, 2012). This only includes fast feedback processes (e.g., clouds, lapse rate, snow, sea ice). Our early Cenozoic BWT are however not only determined by $CO_2$ and short-term climate responses, but also incorporate effects of slower geological feedback processes such as changing paleogeography and growth/decay of continental ice sheets. Hence, we can only interpret our temperatures into the frame of so-called Earth System Sensitivity (Lunt et al., 2010; Pagani et al., 2010; PALAEOSENS, 2012; Royer et al., 2012; Feng et al., 2020; Ring et al., 2022).

The coevolution of BWT (relative changes are representative for similar change in GMST) and atmospheric $CO_2$ through the Cenozoic is displayed in Figure 3. The Paleocene data is absent in this compilation because no $CO_2$ level reconstructions have been published yet for this epoch. In addition to our Eocene clumped isotope data from the South Atlantic, we have added other $\Delta_{47}$-based BWT reconstructions in different ocean basins across younger intervals in the Cenozoic (Figure 3). We exclude Cenozoic $\Delta_{47}$-based temperatures from the relatively smaller North Atlantic basin (Meckler et al., 2022; Braaten et al., 2023) because it periodically exhibits temperature offsets compared to other ocean basins. In addition to the North-South Atlantic temperature differences observed in our early Cenozoic study (Figure 1), BWT reconstructions from the more recent mid-Pliocene indicate that the North Atlantic was >4 °C warmer than the Pacific during this period (Braaten et al., 2023). These findings suggest that additional factors, such as changes in ocean circulation, influenced North Atlantic BWTs beyond the global forcing of $pCO_2$ levels.

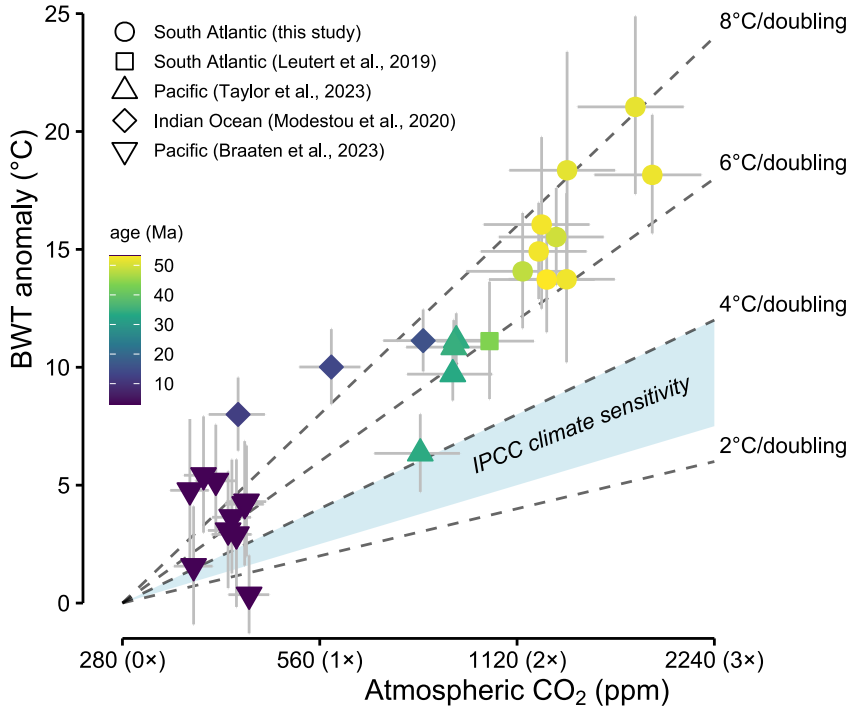


**Figure 3.** Earth System Sensitivity across the Cenozoic based on clumped isotope-based BWTs. The compilation includes BWTs from the Eocene in the South Atlantic (ODP Sites 1262/1263) (this study, Leutert et al., 2019), the Eocene-Oligocene Transition in the Eastern Pacific (ODP Site 1218 and IODP Sites U1333/U1334) (Taylor et al., 2023), the Miocene in the Indian Ocean (ODP Site 761) (Modestou et al., 2020), and the Pliocene in the Eastern Pacific (ODP Site 849) (Braaten et al., 2023). The pre-industrial BWT is set at 0 °C. The lightblue shading indicates the climate sensitivity used by the IPCC (Collins et al., 2013; Sherwood et al., 2020; Forster et al., 2021).

The Cenozoic data compilation shows a strong relationship between atmospheric $CO_2$ and BWT on long time scales. The $CO_2$ is plotted on a logarithmic scale, and the slopes of the dashed lines therefore represent different magnitudes of Earth System Sensitivity. Our inferred Earth System Sensitivity across the Cenozoic generally falls within the range of 6 to 8 °C, a similar result to previous modelling work (Zhu et al., 2019) and sea surface temperature proxy data (Tierney et al., 2022; CenCO2PIP, 2023). This is considerably higher than the estimated range in present-day Equilibrium Climate Sensitivity, recently narrowed to 2.5 to 4.0 °C (best estimate 3.0 °C) in AR6 of the Intergovernmental Panel on Climate Change (IPCC) (Collins et al., 2013; Sherwood et al., 2020; Forster et al., 2021). During the early Cenozoic, when continental ice was absent, high Earth System Sensitivity might have been controlled by fast cloud feedbacks or non-$CO_2$ greenhouse gasses that are stronger in hothouse worlds than they are our modern colder climate system (Zhu et al., 2019). In other words, these additional processes appear to play a key role in amplifying $CO_2$-induced warmth, supporting a climate state dependency of climate sensitivity. Such state dependency of climate sensitivity may have major implications for the IPCC projections of future global warming, as these currently follow the typically lower estimated climate sensitivity.

## Methods

### Approach for BWT reconstruction from $\Delta_{47}$

A downside of measuring clumped isotopes in comparison to other proxies is that it suffers from analytical uncertainty arising from the extremely low natural abundance of $^{13}C$–$^{18}O$ bonds within carbonate ions and the low temperature sensitivity of this proxy (~0.0045‰ /°C) (Ghosh et al., 2006; Schmid & Bernasconi, 2010). Numerous replicate measurements of the same sample need to be averaged to obtain the precision required for paleotemperature reconstructions (Huntington et al., 2009; Meckler et al., 2014; Fernandez et al., 2017; de Winter et al., 2021). Therefore, clumped isotope analysis demands much larger sample sizes in comparison to $\delta^{18}O$ and $\delta^{13}C$ (Zachos et al., 2001, 2008; Littler et al., 2014; Lauretano et al., 2015, 2016, 2018; Westerhold et al., 2018, 2020), and Mg/Ca measurements (Lear et al., 2000, 2010, 2015; Tripati & Elderfield, 2005; Cramer et al., 2011), which is inconvenient when working with ocean sediments that contain limited quantities of a given foraminiferal species.

While foraminiferal $\delta^{18}O$ and Mg/Ca can be used to generate high resolution records, our clumped isotope-based temperatures represent the mean of $\Delta_{47}$ measurements obtained from multiple neighbouring samples, resulting in averaging (binning) of data in intervals of 100–400 kyrs. Using this approach, we were able to generate 12 new BWT bins across the studied interval at the Walvis Ridge. The Paleocene and Eocene isotope data are derived from ODP Site 1262 (paleowater depth ~3600 m) and ODP Site 1263 (paleowater depth ~1500 m), respectively (Zachos et al., 2004, 2005).

As well documented, the early Eocene hothouse also knew periodical occurrences of multiple short-lived global warming events, the so-called hyperthermals (Lourens et al., 2005; Tripati & Elderfield, 2005; Zachos et al., 2005, 2010; Sluijs et al., 2006, 2009, 2011; Stap et al., 2010; Sexton et al., 2011; Kirtland Turner et al., 2014; Frieling et al., 2018; Lauretano et al., 2015, 2016, 2018; Harper et al., 2018; Westerhold et al., 2018; Fokkema et al., 2024a; Fokkema et al., 2024b; Kegel, Fokkema et al., 2025). To primarily capture changes in background climate state, we sampled intervals for our clumped isotope temperature bins that exhibit on average relatively high $\delta^{18}O_b$ and high $\delta^{13}C_b$ (background-related) values. In contrast, the hyperthermal events are recorded by negative excursions in high-resolution $\delta^{18}O_b$ and $\delta^{13}C_b$ records of Sites 1262 and 1263 (Stap et al., 2010; Littler et al., 2014; Lauretano et al., 2015, 2016, 2018). Note that early Eocene hyperthermal BWTs are expected to be approximately 3 °C warmer than the background conditions (Agterhuis et al., 2022).

### Sample preparation

Samples of each approximately 12 CC were first freeze-dried. Hereafter, they were washed over sieves to separate the sediment into three size fractions (>38 µm, >63 µm and >150 µm) and subsequently oven-dried at 40 °C overnight. The largest fraction (>150 µm) was then dry sieved to >212 µm from which the benthic foraminiferal tests were picked. We picked several species or genera, specifically *Nuttallides truempyi*, *Oridorsalis umbonatus*, *Cibicidoides* spp, and additionally *Hanzawaia spp.* for some samples in the ~48 Ma bin (Supplementary Figure S3). We generated Scanning Electron Microscope (SEM) images of a few benthic foraminiferal specimens to assess the preservation state (Supplementary Figure S4). Clearly, there are some signs of recrystallization, such as crystals of secondary calcite growing on the foraminiferal tests. However, studies have not found an impact of diagenetic overprinting on the stable and clumped isotope temperature signal of benthic foraminifera, probably because most of the recrystallization occurs during early burial at the seafloor and would therefore record the same temperatures as the original calcite (Edgar et al., 2013; Voigt et al., 2015, 2016; Stolper et al., 2018; Leutert et al., 2019; Modestou et al., 2020).

Prior to isotope analysis, the benthic foraminifera were cleaned to remove any potential adhering particles and infillings (calcareous nannofossils, organic matter and clays). For each species, the specimens were gently cracked between two glass slides to open the test chambers. In case of low abundance, foraminifers (same species/genera) of neighbouring samples were combined to obtain sufficient material for an isotope measurement (10–20 individuals). Hereafter, the foraminiferal fragments were ultrasonicated at least two times for 60 seconds in deionised water. After each ultrasonication step, the test fragments were rinsed with deionized water for at least two times until the solute was clear and no longer cloudy and the fragments displayed a glassy look under the microscope. Subsequently, after cleaning, the samples were dried at room temperature for two days. Finally, the monospecific samples were weighed and then measured for their $\delta^{18}O$, $\delta^{13}C$, and $\Delta_{47}$ composition.

**Stable and clumped isotope analysis**

In total, we carried out 987 successful stable and clumped isotope measurements of foraminifer samples between April 2021 and August 2023. The setup and procedures are the same as in Agterhuis et al., 2022, which generally follows previous studies (Meckler et al., 2014; Müller et al., 2017).

A detailed description of the analytical methods and data processing can be found in the Supplementary Information. All isotope analyses ($\delta^{18}O$, $\delta^{13}C$, $\Delta_{47}$) were performed using a *Thermo Fisher Scientific MAT 253 Plus* gas source isotope mass spectrometer coupled to a *Thermo Fisher Scientific Kiel IV* carbonate preparation device (Thermo Fisher Scientific, Bremen, Germany) (Schmid & Bernasconi, 2010) at Utrecht University. The Kiel device has been equipped with a Porapak trap to capture organic contaminants (Schmid et al., 2012).

Replicate measurements of individual samples, weighed in between 70 and 90 µg, were spread out randomly for several weeks or months. Furthermore, we measured three carbonate standards (ETH-1,-2, and -3), which differ in bulk isotopic composition and ordering state of isotopes (Bernasconi et al., 2018, 2021), to correct the stable and clumped isotope measurements of the samples. In addition, two check standards (IAEA-C2 and Merck) were used to monitor the long-term reproducibility of the instrument. Every run on the instrument included a similar number of samples and total carbonate standards, with ETH-3 being the dominant standard that was measured. External reproducibility in $\Delta_{47}$ of the IAEA-C2 standard after correction was 0.042‰ (1 standard deviation). The final $\delta^{13}C$ and $\delta^{18}O$ values (reported relative to the VPDB scale) of IAEA-C2 showed external reproducibility of 0.09‰ and 0.14‰ (1 standard deviation), respectively.

**$\Delta_{47}$-based BWT calculations**

As the relationship between $\Delta_{47}$ and temperature is nonlinear (Anderson et al., 2021; Meinicke et al., 2020, 2021), mean $\Delta_{47}$ values were first determined for each bin before the calculation of temperature. To achieve the necessary precision, we averaged ~30–150 individual final corrected $\Delta_{47}$ measurements for each temperature estimate (Schmid & Bernasconi, 2010; Hu et al., 2014; Meckler et al., 2014; Fernandez et al., 2017; Müller et al., 2017; de Winter et al., 2021). As there seem to be no indications for foraminiferal species-specific effects in clumped isotopes (Peral et al., 2018, 2022; Piasecki et al., 2019; Meinicke et al., 2020), we grouped and averaged the $\Delta_{47}$ values from different species together to generate one temperature estimate. Due to low benthic foraminiferal abundance, we pooled the $\Delta_{47}$ data of multiple neighbouring samples together to obtain this number of measurements. This approach creates a high-resolution $\delta^{18}O$ and $\delta^{13}C$ time series for each clumped isotope bin.

To determine BWT from the mean $\Delta_{47}$ values, we applied a foraminifer-based calibration (Meinicke et al., 2020) recalculated to the InterCarb-Carbon Dioxide Equilibrium Scale (I-CDES) in Meinicke et al., 2021 using the updated values of the carbonate standards (Bernasconi et al., 2021) (equation 1). This composite calibration is based on various planktic and benthic foraminiferal $\Delta_{47}$ datasets derived from sediment core tops (Peral et al., 2018; Piasecki et al., 2019; Meinicke et al., 2020) and has been applied in many paleoceanographic studies (Leutert et al., 2020, 2021; Modestou et al., 2020; Agterhuis et al., 2022; Meckler et al., 2022; Hou et al., 2023; Taylor et al., 2023; Braaten et al., 2024). We prefer this equation over the foraminifer-based calibration by Däeron & Gray, 2023. Their regression yields BWT approximately 2–3 °C lower across the Cenozoic, resulting in absolute values as low as −3°C during the Pleistocene, which are physically implausible. These outcomes might suggest potential issues in their approach for estimating calcification temperatures from planktic foraminifera in core tops. Therefore, we consider the calibration by Meinicke et al., 2020, 2021 to be more accurate.

$\Delta_{47}(\text{I-CDES}_{90°C}) = (0.0397\pm0.0011) \times 10^6 / T^2 + (0.1518\pm0.0128)$ ($T$ in K) (1)

(Meinicke et al., 2020, recalculated to I-CDES in Meinicke et al., 2021)

For comparison, we have also plotted BWT according to the combined inorganic-biogenic calibration by Anderson et al., 2021 (equation 2) (Supplementary Figure S5), which spans a very wide temperature range of more than 1000 °C.

$\Delta_{47}(\text{I-CDES}_{90°C}) = (0.0391\pm0.0004) \times 10^6 / T^2 + (0.154\pm0.004)$ ($T$ in K) (2)

(Anderson et al., 2021)

Note that our reconstructed BWT are a little lower (~1.9 °C cooler) when using this calibration instead of the foraminifer-based regression from Meinicke et al., 2020, 2021. For our study, we favour the foraminifer-based calibration because it has a large data density in the range of ocean temperatures. Furthermore, it avoids the influence of a few high temperature data points on the calibration slope (Anderson et al., 2021) that seem to suggest that the $\Delta_{47}$-temperature relationship might not follow a linear regression (with $1/T^2$) over a large temperature range (Guo et al., 2009; Meckler et al., 2022).

**$\delta^{18}O_b$-based BWT and $\delta^{18}O_{sw}$ calculations**

To check if our $\delta^{18}O_b$ and $\delta^{13}C_b$ measurements are consistent with previous work (Supplementary Figure S2), we first compiled continuous high-resolution Paleocene and Eocene $\delta^{18}O_b$ and $\delta^{13}C_b$ records solely based on sites from the Walvis Ridge (South Atlantic) from published studies. The CENOGRID composite $\delta^{18}O_b$ and $\delta^{13}C_b$ records (Westerhold et al., 2020) are composed for a large part of these sites. The Paleocene to middle Eocene interval is entirely based on ODP Sites 1262 (Stap et al., 2010; Littler et al., 2014; Barnet al., 2019) and 1263 (McCarren et al., 2008; Stap et a., 2010; Lauretano et al., 2015, 2016, 2018; Thomas et al., 2018; Westerhold et al., 2020), except for the period ~50–48 Ma which contains data from ODP Site 1258 (Demerara Rise, western tropical Atlantic) (Sexton et al., 2011). We removed the $\delta^{18}O_b$ and $\delta^{13}C_b$ data from Site 1258 and replaced it with Walvis Ridge data from Site 1263 (Lauretano et al., 2016, 2018) and Site 1265 (Westerhold et al., 2020). The high-resolution $\delta^{18}O_b$ and $\delta^{13}C_b$ measurements from these studies are all based *N. truempyi*, while we also measured additional species. The oxygen isotopes of *Cibicidoides* are regarded to be close to seawater equilibrium (Marchitto et al., 2014). As such, we first corrected the isotope values of our study and the previously published records for inter-species offsets (vital effects). The isotopes of *N. truempyi* and *O. umbonatus* were converted towards *Cibicidoides* using the correction factors from Katz et al., 2003 [$\delta^{18}O_{Cib} = (\delta^{18}O_{Nutt} + 0.10)/0.89$; $\delta^{13}C_{Cib} = \delta^{13}C_{Nutt} + 0.34$; $\delta^{18}O_{Cib} = \delta^{18}O_{Orid} - 0.28$; $\delta^{13}C_{Cib} = \delta^{13}C_{Orid} + 0.72$]. Our $\delta^{18}O_b$ and $\delta^{13}C_b$ measurements that are based on *Cibicidoides* obviously do

not require correction. Only few $\delta^{18}O_b$ and $\delta^{13}C_b$ measurements were derived from *Hanzawaia spp*, which is a benthic species not commonly measured. Hence, we did not use these values for further calculations.

We calculated BWT for the compiled high-resolution South Atlantic $\delta^{18}O_b$ composite record (Figure 1). Temperatures were obtained using the $\delta^{18}O$-temperature calibration for *Cibicidoides* of Marchitto et al., 2014 (equation 3), which has been applied in previous reconstructions (Cramer et al., 2011; Agterhuis et al., 2022) (see discussions in Cramer et al., 2011 and Marchitto et al., 2014). A fixed value of −1‰ VSMOW was employed for the $\delta^{18}O_{sw}$ based on the assumption of absence of ice sheets in the early Cenozoic (Shackleton, 1986). This regression shows good correspondence with calibrations derived from inorganic calcite (Kim & O'Neil et al., 1997; Bemis et al., 1998).

$$\delta^{18}O_b(‰\ \text{VPDB}) - \delta^{18}O_{sw}(‰\ \text{VSMOW}) + 0.27 = (-0.245\pm0.005) \times T + (0.0011\pm0.0002) \times T^2 + (3.58\pm0.02)\ (T \text{ in } °C) \quad (3)$$

(Marchitto et al., 2014)

Finally, $\delta^{18}O_{sw}$ values were calculated for the bins, which allows us to test the traditional assumptions on $\delta^{18}O_{sw}$ under ice-free conditions. We used the average $\delta^{18}O_b$ (corrected to *Cibicidoides*) of each bin in combination with the mean $\Delta_{47}$-based temperatures in equation 3 to determine the corresponding $\delta^{18}O_{sw}$ values.

**Uncertainties and error propagation**

Uncertainties on the $\Delta_{47}$-based temperatures and calculated $\delta^{18}O_{sw}$ values are reported as 68% and 95% CI. The error bars on the temperatures represent fully propagated analytical (scatter in the group of $\Delta_{47}$ measurements) and calibration uncertainties. Errors were propagated following the conventional error propagation procedure in Huntington et al., 2009 (see the supporting information in their paper for a description of the mathematics), thereby using Matlab scripts that calculate a variance-covariance matrix of the slopes and intercepts of the foraminifer-based calibration (Meinicke et al., 2020; see Agterhuis et al, 2022 for detailed information). Note that most of the uncertainty in the $\Delta_{47}$-based temperatures stems from the low analytical precision of the measurements, while the effect of the calibration uncertainty is very small (~0.11°C in our error bars) (Huntington et al., 2009; Peral et al., 2018; Leutert et al., 2021). To calculate uncertainties on $\delta^{18}O_{sw}$, we used the $\Delta_{47}$-based temperatures at 68% and 95% CI in equation 3 (Modestou et al., 2020; Agterhuis et al., 2022).

**Data availability**

All replicate-level raw isotope data of samples and standards will be provided upon publication in the EarthChem database (https://www.earthchem.org/) including information regarding the correction procedures (similar to

Agterhuis et al., 2022 and Meckler et al., 2022). The final sample-averaged isotope data, temperatures and $\delta^{18}O_{sw}$ values are reported in Supplementary Data 1.

**References**


1. Agterhuis, T., Ziegler, M., de Winter, N. J. & Lourens, L. J. Warm deep-sea temperatures across Eocene Thermal Maximum 2 from clumped isotope thermometry. *Commun. Earth Environ.* **3**, 1–9 (2022).
2. Anagnostou, E. et al. Changing atmospheric $CO_2$ concentration was the primary driver of early Cenozoic climate. *Nature* **533**, 380–384 (2016).
3. Anagnostou, E. et al. Proxy evidence for state-dependence of climate sensitivity in the Eocene greenhouse. *Nat. Commun.* **11**, 1–9 (2020).
4. Anderson, R. F. et al. Wind-driven upwelling in the Southern Ocean and the deglacial rise in atmospheric $CO_2$. *Science* **323**, 1443–1448 (2009).
5. Anderson, N. T. et al. A unified clumped isotope thermometer calibration (0.5–1,100 °C) using carbonate-based standardization. *Geophys. Res. Lett.* **48**, e2020GL092069 (2021).
6. Barnet, J. S. *et al*. A high-fidelity benthic stable isotope record of late Cretaceous–early Eocene climate change and carbon-cycling. *Paleoceanogr. Paleoclimatol.* **34**, 672–691 (2019).
7. Barr, I. D. *et al*. 60 million years of glaciation in the Transantarctic Mountains. *Nat. Commun.* **13**, 5526 (2022).
8. Batenburg, S. J. et al. Major intensification of Atlantic overturning circulation at the onset of Paleogene greenhouse warmth. *Nat. Commun.* **9**, 1–8 (2018).
9. Bemis, B. E., Spero, H. J., Bijma, J. & Lea, D. W. Reevaluation of the oxygen isotopic composition of planktonic foraminifera: Experimental results and revised paleotemperature equations. *Paleoceanography* **13**, 150–160 (1998).
10. Bernasconi, S. M. *et al*. Background effects on Faraday collectors in gas-source mass spectrometry and implications for clumped isotope measurements. *Rapid Commun. Mass Spectrom.* **27**, 603–612 (2013).
11. Bernasconi, S. M. et al. Reducing uncertainties in carbonate clumped isotope analysis through consistent carbonate-based standardization. *Geochem. Geophys. Geosyst.* **19**, 2895–2914 (2018).
12. Bernasconi, S. M. et al. InterCarb: A community effort to improve interlaboratory standardization of the carbonate clumped isotope thermometer using carbonate standards. *Geochem. Geophys. Geosyst.* **22**, e2020GC009588 (2021).
13. Bijl, P. K. et al. Early Palaeogene temperature evolution of the southwest Pacific Ocean. *Nature* **461**, 776–779 (2009).
14. Bijl, P. K. et al. Eocene cooling linked to early flow across the Tasmanian Gateway. *Proc. Natl Acad. Sci. USA* **110**, 9645–9650 (2013).

15. Billups, K. & Schrag, D. P. Application of benthic foraminiferal Mg/Ca ratios to questions of Cenozoic climate change. *Earth Planet. Sci. Lett.* **209**, 181–195 (2003).
16. Braaten, A. H. *et al*. Limited exchange between the deep Pacific and Atlantic oceans during the warm mid-Pliocene and MIS M2 "glaciation". *Clim. Past* **19**, 2109–2125 (2023).
17. Breitenbach, S. F. et al. Coupled Mg/Ca and clumped isotope analyses of foraminifera provide consistent water temperatures. *Geochim. Cosmochim. Acta* **236**, 283–296 (2018).
18. Broecker, W. & Yu, J. What do we know about the evolution of Mg to Ca ratios in seawater? *Paleoceanography* **26** (2011).
19. Brune, S., Williams, S. E. & Müller, R. D. Potential links between continental rifting, $CO_2$ degassing and climate change through time. *Nat. Geosci.* **10**, 941–946 (2017).
20. Burke, A. & Robinson, L. F. The Southern Ocean's role in carbon exchange during the last deglaciation. *Science* **335**, 557–561 (2012).
21. Burke, K. D. et al. Pliocene and Eocene provide best analogs for near-future climates. *Proc. Natl Acad. Sci. USA* **115**, 13288–13293 (2018).
22. Carter, A., Riley, T. R., Hillenbrand, C. & Rittner, M. Widespread Antarctic glaciation during the late Eocene. *Earth Planet. Sci. Lett.* **458**, 49–57 (2017).
23. Cenozoic CO2 Proxy Integration Project (CenCO2PIP) Consortium. Toward a Cenozoic history of atmospheric $CO_2$. *Science* **382**, eadi5177 (2023).
24. Clark, P. U., Pisias, N. G., Stocker, T. F. & Weaver, A. J. The role of the thermohaline circulation in abrupt climate change. *Nature* **415**, 863–869 (2002).
25. Coggon, R. M., Teagle, D. A., Smith-Duque, C. E., Alt, J. C. & Cooper, M. J. Reconstructing past seawater Mg/Ca and Sr/Ca from mid-ocean ridge flank calcium carbonate veins. *Science* **327**, 1114–1117 (2010).
26. Collins, M. *et al.* Long-term climate change: projections, commitments and irreversibility. *Climate Change 2013: The Physical Science Basis. Contribution of Working Group I to the Fifth Assessment Report of the Intergovernmental Panel on Climate Change* Ch. 12, 1029–1136 (Cambridge Univ. Press, 2013).
27. Conrad, C. P. & Lithgow-Bertelloni, C. Faster seafloor spreading and lithosphere production during the mid-Cenozoic. *Geology* **35**, 29–32 (2007).
28. Cramer, B. S., Toggweiler, J. R., Wright, J. D., Katz, M. E. & Miller, K. G. Ocean overturning since the Late Cretaceous: Inferences from a new benthic foraminiferal isotope compilation. *Paleoceanography* **24**, PA4216 (2009).
29. Cramer, B. S., Miller, K. G., Barrett, P. J. & Wright, J. D. Late Cretaceous–Neogene trends in deep ocean temperature and continental ice volume: Reconciling records of benthic foraminiferal geochemistry ($\delta^{18}O$ and Mg/Ca) with sea level history. *J. Geophys. Res.* **116**, C12023 (2011).

30. Cramwinckel, M. J. et al. Synchronous tropical and polar temperature evolution in the Eocene. *Nature* **559**, 382–386 (2018).
31. Cramwinckel, M. J. et al. A warm, stratified, and restricted Labrador Sea across the Middle Eocene and its climatic optimum. *Paleoceanogr. Paleoclimatol.* **35**, e2020PA003932 (2020).
32. Daëron, M. & Gray, W. R. Revisiting oxygen-18 and clumped isotopes in planktic and benthic foraminifera. *Paleoceanogr. Paleoclimatol.* **38**, e2023PA004660 (2023).
33. Darby, D. A. Ephemeral formation of perennial sea ice in the Arctic Ocean during the middle Eocene. *Nat. Geosci.* **7**, 210–213 (2014).
34. Davies, A. et al. Assessing the impact of aquifer-eustasy on short-term Cretaceous sea-level. *Cretac. Res.* **112**, 104445 (2020).
35. Dennis, K. J., Affek, H. P., Passey, B. H., Schrag, D. P. & Eiler, J. M. Defining an absolute reference frame for 'clumped' isotope studies of $CO_2$. *Geochim. Cosmochim. Acta* **75**, 7117–7131 (2011).
36. Dutton, A., Lohmann, K. & Leckie, R. Data report: stable isotope and Mg/Ca of Paleocene and Eocene foraminifers, ODP Site 1209, Shatsky Rise. *Proc. ODP, Sci. Results* **198**, 1–19 (Ocean Drilling Program, 2005a).
37. Dutton, A., Lohmann, K. C. & Leckie, R. M. Insights from the Paleogene tropical Pacific: Foraminiferal stable isotope and elemental results from Site 1209, Shatsky Rise. *Paleoceanography* **20** (2005b).
38. Edgar, K. M., Pälike, H. & Wilson, P. A. Testing the impact of diagenesis on the $\delta^{18}O$ and $\delta^{13}C$ of benthic foraminiferal calcite from a sediment burial depth transect in the equatorial Pacific. *Paleoceanography* **28**, 468–480 (2013).
39. Ehrmann, W. U. & Mackensen, A. Sedimentological evidence for the formation of an East Antarctic ice sheet in Eocene/Oligocene time. *Palaeogeogr. Palaeoclimatol. Palaeoecol.* **93**, 85–112 (1992).
40. Eiler, J. M. "Clumped-isotope" geochemistry—The study of naturally-occurring, multiply-substituted isotopologues. *Earth Planet. Sci. Lett.* **262**, 309–327 (2007).
41. Eiler, J. M. Paleoclimate reconstruction using carbonate clumped isotope thermometry. *Quat. Sci. Rev.* **30**, 3575–3588 (2011).
42. Elderfield, H., Yu, J., Anand, P., Kiefer, T. & Nyland, B. Calibrations for benthic foraminiferal Mg/Ca paleothermometry and the carbonate ion hypothesis. *Earth Planet. Sci. Lett.* **250**, 633–649 (2006).
43. Eldrett, J. S., Harding, I. C., Wilson, P. A., Butler, E. & Roberts, A. P. Continental ice in Greenland during the Eocene and Oligocene. *Nature* **446**, 176–179 (2007).
44. Evans, D. & Müller, W. Deep time foraminifera Mg/Ca paleothermometry: Nonlinear correction for secular change in seawater Mg/Ca. *Paleoceanography* **27**, PA4205 (2012).

45. Evans, D., Brierley, C., Raymo, M. E., Erez, J. & Müller, W. Planktic foraminifera shell chemistry response to seawater chemistry: Pliocene–Pleistocene seawater Mg/Ca, temperature and sea level change. *Earth Planet. Sci. Lett.* **438**, 139–148 (2016).
46. Evans, D. et al. Eocene greenhouse climate revealed by coupled clumped isotope-Mg/Ca thermometry. *Proc. Natl Acad. Sci. USA* **115**, 1174–1179 (2018a).
47. Evans, D., Müller, W. & Erez, J. Assessing foraminifera biomineralisation models through trace element data of cultures under variable seawater chemistry. *Geochim. Cosmochim. Acta* **236**, 198–217 (2018b).
48. Evans, D., Brugger, J., Inglis, G. N. & Valdes, P. The temperature of the deep ocean is a robust proxy for global mean surface temperature during the Cenozoic. *Paleoceanogr. Paleoclimatol.* **39**, e2023PA004788 (2024).
49. Feng, R., Otto-Bliesner, B. L., Brady, E. C. & Rosenbloom, N. Increased climate response and Earth system sensitivity from CCSM4 to CESM2 in mid-Pliocene simulations. *J. Adv. Model. Earth Syst*. **12**, e2019MS002033 (2020).
50. Fernandez, A. et al. A reassessment of the precision of carbonate clumped isotope measurements: Implications for calibrations and paleoclimate reconstructions. *Geochem. Geophys. Geosyst.* **18**, 4375–4386 (2017).
51. Fokkema, C. D. et al. Polar amplification of orbital-scale climate variability in the early Eocene greenhouse world. *Clim. Past* **20**, 1303–1325 (2024a).
52. Fokkema, C. D., Brinkhuis, H., Peterse, F. & Sluijs, A. Orbital (hydro)climate variability in the ice-free early Eocene Arctic. *Paleoceanogr. Paleoclimatol.* **39**, e2024PA004907 (2024b).
53. Frieling, J. et al. Paleocene–Eocene warming and biotic response in the epicontinental West Siberian Sea. *Geology* **42**, 767–770 (2014).
54. Frieling, J. et al. Tropical Atlantic climate and ecosystem regime shifts during the Paleocene–Eocene Thermal Maximum. *Clim. Past* **14**, 39–55 (2018).
55. Forster, P. *et al.* The Earth's energy budget, climate feedbacks, and climate sensitivity. *Climate Change 2021: The Physical Science Basis. Contribution of Working Group I to the Sixth Assessment Report of the Intergovernmental Panel on Climate Change* Ch. 7, 923–1054 (Cambridge Univ. Press, 2021).
56. Galeotti, S. *et al*. Antarctic Ice Sheet variability across the Eocene-Oligocene boundary climate transition. *Science* **352**, 76–80 (2016).
57. Gaskell, D. E. *et al*. The latitudinal temperature gradient and its climate dependence as inferred from foraminiferal $\delta^{18}O$ over the past 95 million years. *Proc. Natl Acad. Sci. USA* **119**, e2111332119 (2022).
58. Ghosh, P. et al. $^{13}C$–$^{18}O$ bonds in carbonate minerals: A new kind of paleothermometer. *Geochim. Cosmochim. Acta* **70**, 1439–1456 (2006).
59. Goudsmit-Harzevoort, B. *et al*. The relationship between the global mean deep-sea and surface temperature during the early Eocene. *Paleoceanogr. Paleoclimatol.* **38**, e2022PA004532 (2023).

60. Grauel, A. et al. Calibration and application of the 'clumped isotope' thermometer to foraminifera for high-resolution climate reconstructions. *Geochim. Cosmochim. Acta* **108**, 125–140 (2013).
61. Gray, W. R. et al. The effects of temperature, salinity, and the carbonate system on Mg/Ca in Globigerinoides ruber (white): A global sediment trap calibration. *Earth Planet. Sci. Lett.* **482**, 607–620 (2018).
62. Gulick, S. P. *et al*. Initiation and long-term instability of the East Antarctic Ice Sheet. *Nature* **552**, 225–229 (2017).
63. Guo, W., Mosenfelder, J. L., Goddard III, W. A. & Eiler, J. M. Isotopic fractionations associated with phosphoric acid digestion of carbonate minerals: Insights from first-principles theoretical modeling and clumped isotope measurements. *Geochim. Cosmochim. Acta* **73**, 7203–7225 (2009).
64. Guo, W. Kinetic clumped isotope fractionation in the DIC-$H_2O$-$CO_2$ system: patterns, controls, and implications. *Geochim. Cosmochim. Acta* **268**, 230–257 (2020).
65. Gutjahr, M. *et al*. Very large release of mostly volcanic carbon during the Palaeocene–Eocene Thermal Maximum. *Nature* **548**, 573–577 (2017).
66. Hansen, J., Sato, M., Russell, G. & Kharecha, P. Climate sensitivity, sea level and atmospheric carbon dioxide. *Philos. Trans. R. Soc. A* **371**, 20120294 (2013).
67. Harper, D. T. et al. Subtropical sea-surface warming and increased salinity during Eocene Thermal Maximum 2. *Geology* **46**, 187–190 (2018).
68. Harper, D. T. *et al*. The magnitude of surface ocean acidification and carbon release during Eocene Thermal Maximum 2 (ETM-2) and the Paleocene-Eocene Thermal Maximum (PETM). *Paleoceanogr. Paleoclimatol.* **35**, e2019PA003699 (2020).
69. He, B., Olack, G. A. & Colman, A. S. Pressure baseline correction and high-precision $CO_2$ clumped-isotope ($\Delta_{47}$) measurements in bellows and micro-volume modes. *Rapid Commun. Mass Spectrom.* **26**, 2837–2853 (2012).
70. Hill, P. S., Tripati, A. K. & Schauble, E. A. Theoretical constraints on the effects of pH, salinity, and temperature on clumped isotope signatures of dissolved inorganic carbon species and precipitating carbonate minerals. *Geochim. Cosmochim. Acta* **125**, 610–652 (2014).
71. Hilting, A. K., Kump, L. R. & Bralower, T. J. Variations in the oceanic vertical carbon isotope gradient and their implications for the Paleocene-Eocene biological pump. *Paleoceanography* **23** (2008).
72. Hohbein, M. W., Sexton, P. F. & Cartwright, J. A. Onset of North Atlantic Deep Water production coincident with inception of the Cenozoic global cooling trend. *Geology* **40**, 255–258 (2012).
73. Hollis, C. J. et al. Early Paleogene temperature history of the Southwest Pacific Ocean: Reconciling proxies and models. *Earth Planet. Sci. Lett.* **349**, 53–66 (2012).

74. Hollis, C. J. et al. The DeepMIP contribution to PMIP4: methodologies for selection, compilation and analysis of latest Paleocene and early Eocene climate proxy data, incorporating version 0.1 of the DeepMIP database. *Geosci. Model Dev.* **12**, 3149–3206 (2019).
75. Horita, J., Zimmermann, H. & Holland, H. D. Chemical evolution of seawater during the Phanerozoic: Implications from the record of marine evaporites. *Geochim. Cosmochim. Acta* **66**, 3733–3756 (2002).
76. Hou, S. et al. Reconciling Southern Ocean fronts equatorward migration with minor Antarctic ice volume change during Miocene cooling. *Nat. Commun.* **14**, 7230 (2023).
77. Hu, B. et al. A modified procedure for gas-source isotope ratio mass spectrometry: The long-integration dual-inlet (LIDI) methodology and implications for clumped isotope measurements. *Rapid Commun. Mass Spectrom.* **28**, 1413–1425 (2014).
78. Huck, C. E., van de Flierdt, T., Bohaty, S. M. & Hammond, S. J. Antarctic climate, Southern Ocean circulation patterns, and deep water formation during the Eocene. *Paleoceanography* **32**, 674–691 (2017).
79. Huntington, K. W. et al. Methods and limitations of 'clumped' $CO_2$ isotope ($\Delta_{47}$) analysis by gas-source isotope ratio mass spectrometry. *J. Mass Spectrom.* **44**, 1318–1329 (2009).
80. Huntington, K. W. & Petersen, S. V. Frontiers of carbonate clumped isotope thermometry. *Annu. Rev. Earth Planet. Sci.* **51**, 611–641 (2023).
81. Jaffrés, J. B., Shields, G. A. & Wallmann, K. The oxygen isotope evolution of seawater: A critical review of a long-standing controversy and an improved geological water cycle model for the past 3.4 billion years. *Earth-Sci. Rev.* **83**, 83–122 (2007).
82. Judd, E. J., Bhattacharya, T. & Ivany, L. C. A dynamical framework for interpreting ancient sea surface temperatures. *Geophys. Res. Lett.* **47**, e2020GL089044 (2020).
83. Katz, M. E. et al. Early Cenozoic benthic foraminiferal isotopes: Species reliability and interspecies correction factors. *Paleoceanography* **18**, 1024 (2003).
84. Kegel, A. H. *et al*. Global warming and equatorial Atlantic paleoceanographic changes during early Eocene carbon cycle perturbation V. *Paleoceanogr. Paleoclimatol.* **40**, e2024PA004913 (2025).
85. Kelson, J. R., Huntington, K. W., Schauer, A. J., Saenger, C. & Lechler, A. R. Toward a universal carbonate clumped isotope calibration: Diverse synthesis and preparatory methods suggest a single temperature relationship. *Geochim. Cosmochim. Acta* **197**, 104–131 (2017).
86. Kender, S., Yu, J. & Peck, V. L. Deep ocean carbonate ion increase during mid Miocene $CO_2$ decline. *Sci. Rep.* **4**, 4187 (2014).
87. Kim, S. & O'Neil, J. R. Equilibrium and nonequilibrium oxygen isotope effects in synthetic carbonates. *Geochim. Cosmochim. Acta* **61**, 3461–3475 (1997).
88. Kirtland Turner, S., Sexton, P. F., Charles, C. D. & Norris, R. D. Persistence of carbon release events through the peak of early Eocene global warmth. *Nat. Geosci.* **7**, 748–751 (2014).

89. Kirtland Turner, S. *et al*. Sensitivity of ocean circulation to warming during the Early Eocene greenhouse. *Proc. Natl Acad. Sci. USA* **121**, e2311980121 (2024).
90. Klages, J. P. *et al*. Ice sheet–free West Antarctica during peak early Oligocene glaciation. *Science* **385**, 322–327 (2024).
91. Kocken, I. J. et al. North Atlantic temperature change across the Eocene-Oligocene transition from clumped isotopes. *Paleoceanogr. Paleoclimatol.* **39**, e2023PA004809 (2024).
92. Kostov, Y., Armour, K. C. & Marshall, J. Impact of the Atlantic meridional overturning circulation on ocean heat storage and transient climate change. *Geophys. Res. Lett.* **41**, 2108–2116 (2014).
93. Inglis, G. N. et al. Descent toward the Icehouse: Eocene sea surface cooling inferred from GDGT distributions. *Paleoceanography* **30**, 1000–1020 (2015).
94. Inglis, G. N. *et al*. Global mean surface temperature and climate sensitivity of the EECO, PETM and latest Paleocene. *Clim. Past* **16**, 1953–1968 (2020).
95. Lauvset, S. K. *et al*. Processes driving global interior ocean pH distribution. *Global Biogeochem. Cycles* **34**, e2019GB006229 (2020).
96. Lauretano, V., Littler, K., Polling, M., Zachos, J. C. & Lourens, L. J. Frequency, magnitude and character of hyperthermal events at the onset of the Early Eocene Climatic Optimum. *Clim. Past* **11**, 1313–1324 (2015).
97. Lauretano, V., Hilgen, F. J., Zachos, J. C. & Lourens, L. J. Astronomically tuned age model for the early Eocene carbon isotope events: A new high-resolution $\delta^{13}C_{benthic}$ record of ODP Site 1263 between ~49 and ~54 Ma. *Newsl. Stratigr.* **49**, 383–400 (2016).
98. Lauretano, V., Zachos, J. C. & Lourens, L. J. Orbitally paced carbon and deep-sea temperature changes at the peak of the Early Eocene Climatic Optimum. *Paleoceanogr. Paleoclimatol.* **33**, 1050–1065 (2018).
99. Lear, C. H., Elderfield, H. & Wilson, P. A. Cenozoic deep-sea temperatures and global ice volumes from Mg/Ca in benthic foraminiferal calcite. *Science* **287**, 269–272 (2000).
100. Lear, C. H., Rosenthal, Y. & Slowey, N. Benthic foraminiferal Mg/Ca-paleothermometry: A revised core-top calibration. *Geochim. Cosmochim. Acta* **66**, 3375–3387 (2002).
101. Lear, C. H., Mawbey, E. M. & Rosenthal, Y. Cenozoic benthic foraminiferal Mg/Ca and Li/Ca records: Toward unlocking temperatures and saturation states. *Paleoceanography* **25** (2010).
102. Lear, C. H. et al. Neogene ice volume and ocean temperatures: Insights from infaunal foraminiferal Mg/Ca paleothermometry. *Paleoceanography* **30**, 1437–1454 (2015).
103. Lee, C. A. et al. Continental arc–island arc fluctuations, growth of crustal carbonates, and long-term climate change. *Geosphere* **9**, 21–36 (2013).
104. Leutert, T. J. et al. Sensitivity of clumped isotope temperatures in fossil benthic and planktic foraminifera to diagenetic alteration. *Geochim. Cosmochim. Acta* **257**, 354–372 (2019).

105. Leutert, T. J., Auderset, A., Martínez-García, A., Modestou, S. & Meckler, A. N. Coupled Southern Ocean cooling and Antarctic ice sheet expansion during the middle Miocene. *Nat. Geosci.* **13**, 634–639 (2020).

106. Leutert, T. J., Modestou, S., Bernasconi, S. M. & Meckler, A. N. Southern Ocean bottom-water cooling and ice sheet expansion during the middle Miocene climate transition. *Clim. Past* **17**, 2255–2271 (2021).

107. Littler, K., Röhl, U., Westerhold, T. & Zachos, J. C. A high-resolution benthic stable-isotope record for the South Atlantic: Implications for orbital-scale changes in Late Paleocene–Early Eocene climate and carbon cycling. *Earth Planet. Sci. Lett.* **401**, 18–30 (2014).

108. Lourens, L. J. et al. Astronomical pacing of late Palaeocene to early Eocene global warming events. *Nature* **435**, 1083–1087 (2005).

109. Lowenstein, T. K., Timofeeff, M. N., Brennan, S. T., Hardie, L. A. & Demicco, R. V. Oscillations in Phanerozoic seawater chemistry: Evidence from fluid inclusions. *Science* **294**, 1086–1088 (2001).

110. Lunt, D. J. et al. Earth system sensitivity inferred from Pliocene modelling and data. *Nat. Geosci.* **3**, 60–64 (2010).

111. Lunt, D. J. et al. DeepMIP: Model intercomparison of early Eocene climatic optimum (EECO) large-scale climate features and comparison with proxy data. *Clim. Past* **17**, 203–227 (2021).

112. Marchitto, T. M., Bryan, S. P., Curry, W. B. & McCorkle, D. C. Mg/Ca temperature calibration for the benthic foraminifer Cibicidoides pachyderma. *Paleoceanography* **22** (2007).

113. Marchitto, T. M. et al. Improved oxygen isotope temperature calibrations for cosmopolitan benthic foraminifera. *Geochim. Cosmochim. Acta* **130**, 1–11 (2014).

114. McCarren, H., Thomas, E., Hasegawa, T., Röhl, U. & Zachos, J. C. Depth dependency of the Paleocene-Eocene carbon isotope excursion: Paired benthic and terrestrial biomarker records (Ocean Drilling Program Leg 208, Walvis Ridge). *Geochem. Geophys. Geosyst.* **9** (2008).

115. McCrea, J. M. On the isotopic chemistry of carbonates and a paleotemperature scale. *J. Chem. Phys.* **18**, 849–857 (1950).

116. Meckler, A. N., Ziegler, M., Millán, M. I., Breitenbach, S. F. & Bernasconi, S. M. Long-term performance of the Kiel carbonate device with a new correction scheme for clumped isotope measurements. *Rapid Commun. Mass Spectrom.* **28**, 1705–1715 (2014).

117. Meckler, A. N. et al. Cenozoic evolution of deep ocean temperature from clumped isotope thermometry. *Science* **377**, 86–90 (2022).

118. Meinicke, N. et al. A robust calibration of the clumped isotopes to temperature relationship for foraminifers. *Geochim. Cosmochim. Acta* **270**, 160–183 (2020).

119. Meinicke, N., Reimi, M. A., Ravelo, A. C. & Meckler, A. N. Coupled Mg/Ca and clumped isotope measurements indicate lack of substantial mixed layer cooling in the Western Pacific Warm Pool during the last ~5 million years. *Paleoceanogr. Paleoclimatol.* **36**, e2020PA004115 (2021).

120. Miller, K. G. et al. Cenozoic sea-level and cryospheric evolution from deep-sea geochemical and continental margin records. *Sci. Adv.* **6**, eaaz1346 (2020).

121. Modestou, S. E., Leutert, T. J., Fernandez, A., Lear, C. H. & Meckler, A. N. Warm middle Miocene Indian Ocean bottom water temperatures: comparison of clumped isotope and Mg/Ca-based estimates. *Paleoceanogr. Paleoclimatol.* **35**, e2020PA003927 (2020).

122. Müller, I. A. et al. Carbonate clumped isotope analyses with the long-integration dual-inlet (LIDI) workflow: Scratching at the lower sample weight boundaries. *Rapid Commun. Mass Spectrom.* **31**, 1057–1066 (2017).

123. Müller, R. D., Sdrolias, M., Gaina, C., Steinberger, B. & Heine, C. Long-term sea-level fluctuations driven by ocean basin dynamics. *Science* **319**, 1357–1362 (2008).

124. Pagani, M., Liu, Z., LaRiviere, J. & Ravelo, A. C. High Earth-system climate sensitivity determined from Pliocene carbon dioxide concentrations. *Nat. Geosci.* **3**, 27–30 (2010).

125. PALAEOSENS Project Members. Making sense of palaeoclimate sensitivity. *Nature* **491**, 683–691 (2012).

126. Passchier, S., Ciarletta, D. J., Miriagos, T. E., Bijl, P. K. & Bohaty, S. M. An Antarctic stratigraphic record of stepwise ice growth through the Eocene-Oligocene transition. *Geol. Soc. Am. Bull.* **129**, 318–330 (2017).

127. Pearson, P. N. *et al*. Stable warm tropical climate through the Eocene Epoch. *Geology* **35**, 211–214 (2007).

128. Pearson, P. N. Oxygen isotopes in foraminifera: overview and historical review. *Reconstructing Earth's Deep-Time Climate—The State of the Art in 2012*. *Paleontological Society Papers* **18**, 1–38 (Paleontological Society, 2012).

129. Penman, D. E., Hönisch, B., Zeebe, R. E., Thomas, E. & Zachos, J. C. Rapid and sustained surface ocean acidification during the Paleocene-Eocene Thermal Maximum. *Paleoceanography* **29**, 357–369 (2014).

130. Peral, M. et al. Updated calibration of the clumped isotope thermometer in planktonic and benthic foraminifera. *Geochim. Cosmochim. Acta* **239**, 1–16 (2018).

131. Peral, M. et al. On the combination of the planktonic foraminiferal Mg/Ca, clumped ($\Delta_{47}$) and conventional ($\delta^{18}O$) stable isotope paleothermometers in palaeoceanographic studies. *Geochim. Cosmochim. Acta* **339**, 22–34 (2022).

132. Piasecki, A. et al. Application of clumped isotope thermometry to benthic foraminifera. *Geochem. Geophys. Geosyst.* **20**, 2082–2090 (2019).

133. Pross, J. et al. Persistent near-tropical warmth on the Antarctic continent during the early Eocene epoch. *Nature* **488**, 73–77 (2012).

134. Rae, J. W. et al. Atmospheric $CO_2$ over the past 66 million years from marine archives. *Annu. Rev. Earth Planet. Sci.* **49**, 599–631 (2021).

135. Rathmann, S. & Kuhnert, H. Carbonate ion effect on Mg/Ca, Sr/Ca and stable isotopes on the benthic foraminifera Oridorsalis umbonatus off Namibia. *Mar. Micropaleontol.* **66**, 120–133 (2008).

136. Ravelo, A. C. & Hillaire-Marcel, C. The use of oxygen and carbon isotopes of foraminifera in paleoceanography. *Proxies in Late Cenozoic Paleoceanography*. *Developments in Marine Geology* **1**, 735–764 (Elsevier, 2007).
137. Raymo, M. E., Kozdon, R., Evans, D., Lisiecki, L. & Ford, H. L. The accuracy of mid-Pliocene $\delta^{18}O$-based ice volume and sea level reconstructions. *Earth-Sci. Rev.* **177**, 291–302 (2018).
138. Reagan, M. K. et al. The geology of the southern Mariana fore-arc crust: Implications for the scale of Eocene volcanism in the western Pacific. *Earth Planet. Sci. Lett.* **380**, 41–51 (2013).
139. Ring, S. J., Mutz, S. G. & Ehlers, T. A. Cenozoic proxy constraints on Earth system sensitivity to greenhouse gases. *Paleoceanogr. Paleoclimatol.* **37**, e2021PA004364 (2022).
140. Rodríguez-Sanz, L. et al. Penultimate deglacial warming across the Mediterranean Sea revealed by clumped isotopes in foraminifera. *Sci. Rep.* **7**, 16572 (2017).
141. Rohling, E. J. *et al*. Reconciling the apparent discrepancy between Cenozoic deep-sea temperatures from proxies and from benthic oxygen isotope deconvolution. *Paleoceanogr. Paleoclimatol.* **39**, e2024PA004872 (2024).
142. Rose, B. E. & Ferreira, D. Ocean heat transport and water vapor greenhouse in a warm equable climate: A new look at the low gradient paradox. *J. Clim.* **26**, 2117–2136 (2013).
143. Royer, D. L., Pagani, M. & Beerling, D. J. Geobiological constraints on Earth system sensitivity to $CO_2$ during the Cretaceous and Cenozoic. *Geobiology* **10**, 298–310 (2012).
144. Sames, B., Wagreich, M., Conrad, C. P. & Iqbal, S. Aquifer-eustasy as the main driver of short-term sea-level fluctuations during Cretaceous hothouse climate phases. *Geol. Soc. Lond. Spec. Publ.* **498**, 9–38 (2020).
145. Schauble, E. A., Ghosh, P. & Eiler, J. M. Preferential formation of $^{13}C$–$^{18}O$ bonds in carbonate minerals, estimated using first-principles lattice dynamics. *Geochim. Cosmochim. Acta* **70**, 2510–2529 (2006).
146. Scher, H. D., Bohaty, S. M., Zachos, J. C. & Delaney, M. L. Two-stepping into the icehouse: East Antarctic weathering during progressive ice-sheet expansion at the Eocene–Oligocene transition. *Geology* **39**, 383–386 (2011).
147. Schmid, T. W. & Bernasconi, S. M. An automated method for 'clumped-isotope' measurements on small carbonate samples. *Rapid Commun. Mass Spectrom.* **24**, 1955–1963 (2010).
148. Schmid, T. W., Radke, J. & Bernasconi, S. M. Clumped-isotope measurements on small carbonate samples with a Kiel IV carbonate device and a MAT 253 mass spectrometer. *Appl. Note* **30233**, (Thermo Fisher, 2012).
149. Sexton, P. F. et al. Eocene global warming events driven by ventilation of oceanic dissolved organic carbon. *Nature* **471**, 349–352 (2011).
150. Shackleton, N. J. Paleogene stable isotope events. *Palaeogeogr. Palaeoclimatol. Palaeoecol.* **57**, 91–102 (1986).
151. Sherwood, S. C. et al. An assessment of Earth's climate sensitivity using multiple lines of evidence. *Rev. Geophys.* **58**, e2019RG000678 (2020).

152. Sluijs, A. et al. Subtropical Arctic Ocean temperatures during the Palaeocene/Eocene Thermal Maximum. *Nature* **441**, 610–613 (2006).
153. Sluijs, A. et al. Warm and wet conditions in the Arctic region during Eocene Thermal Maximum 2. *Nat. Geosci.* **2**, 777–780 (2009).
154. Sluijs, A. et al. Southern ocean warming, sea level and hydrological change during the Paleocene-Eocene thermal maximum. *Clim. Past* **7**, 47–61 (2011).
155. Spero, H. J., Bijma, J., Lea, D. W. & Bemis, B. E. Effect of seawater carbonate concentration on foraminiferal carbon and oxygen isotopes. *Nature* **390**, 497–500 (1997).
156. Spray, J. F. *et al*. North Atlantic evidence for a unipolar icehouse climate state at the Eocene-Oligocene Transition. *Paleoceanogr. Paleoclimatol.* **34**, 1124–1138 (2019).
157. Srokosz, M. et al. Past, present, and future changes in the Atlantic meridional overturning circulation. *Bull. Am. Meteorol. Soc.* **93**, 1663–1676 (2012).
158. St. John, K. Cenozoic ice-rafting history of the central Arctic Ocean: Terrigenous sands on the Lomonosov Ridge. *Paleoceanography* **23** (2008).
159. Stap, L. *et al*. High-resolution deep-sea carbon and oxygen isotope records of Eocene Thermal Maximum 2 and H2. *Geology* **38**, 607–610 (2010).
160. Stickley, C. E. et al. Evidence for middle Eocene Arctic sea ice from diatoms and ice-rafted debris. *Nature* **460**, 376–379 (2009).
161. Stolper, D. A., Eiler, J. M. & Higgins, J. A. Modeling the effects of diagenesis on carbonate clumped-isotope values in deep-and shallow-water settings. *Geochim. Cosmochim. Acta* **227**, 264–291 (2018).
162. Storey, M., Duncan, R. A. & Tegner, C. Timing and duration of volcanism in the North Atlantic Igneous Province: Implications for geodynamics and links to the Iceland hotspot. *Chem. Geol.* **241**, 264-281 (2007).
163. Tang, J., Dietzel, M., Fernandez, A., Tripati, A. K. & Rosenheim, B. E. Evaluation of kinetic effects on clumped isotope fractionation ($\Delta_{47}$) during inorganic calcite precipitation. *Geochim. Cosmochim. Acta* **134**, 120–136 (2014).
164. Taylor, V. E., Wilson, P. A., Bohaty, S. M. & Meckler, A. N. Transient Deep Ocean Cooling in the Eastern Equatorial Pacific Ocean at the Eocene-Oligocene Transition. *Paleoceanogr. Paleoclimatol.* **38**, e2023PA004650 (2023).
165. Thomas, D. J., Bralower, T. J. & Jones, C. E. Neodymium isotopic reconstruction of late Paleocene–early Eocene thermohaline circulation. *Earth Planet. Sci. Lett.* **209**, 309–322 (2003).
166. Thomas, D. J., Korty, R., Huber, M., Schubert, J. A. & Haines, B. Nd isotopic structure of the Pacific Ocean 70–30 Ma and numerical evidence for vigorous ocean circulation and ocean heat transport in a greenhouse world. *Paleoceanography* **29**, 454–469 (2014).

167. Thomas, E. *et al.* Early Eocene thermal maximum 3: Biotic response at Walvis ridge (SE Atlantic ocean). *Paleoceanogr. Paleoclimatol.* **33**, 862–883 (2018).
168. Tierney, J. E. et al. Spatial patterns of climate change across the Paleocene–Eocene Thermal Maximum. *Proc. Natl Acad. Sci. USA* **119**, e2205326119 (2022).
169. Trenberth, K. E. & Caron, J. M. Estimates of meridional atmosphere and ocean heat transports. *J. Clim.* **14**, 3433–3443 (2001).
170. Tripati, A. K. et al. Tropical sea-surface temperature reconstruction for the early Paleogene using Mg/Ca ratios of planktonic foraminifera. *Paleoceanography* **18** (2003).
171. Tripati, A. & Elderfield, H. Deep-sea temperature and circulation changes at the Paleocene-Eocene Thermal Maximum. *Science* **308**, 1894–1898 (2005).
172. Tripati, A. K. et al. $^{13}C$–$^{18}O$ isotope signatures and 'clumped isotope' thermometry in foraminifera and coccoliths. *Geochim. Cosmochim. Acta* **74**, 5697–5717 (2010).
173. Tripati, A. K. et al. Beyond temperature: Clumped isotope signatures in dissolved inorganic carbon species and the influence of solution chemistry on carbonate mineral composition. *Geochim. Cosmochim. Acta* **166**, 344–371 (2015).
174. Tripati, A. & Darby, D. Evidence for ephemeral middle Eocene to early Oligocene Greenland glacial ice and pan-Arctic sea ice. *Nat. Commun.* **9**, 1–11 (2018).
175. Uchikawa, J. & Zeebe, R. E. Examining possible effects of seawater pH decline on foraminiferal stable isotopes during the Paleocene-Eocene Thermal Maximum. *Paleoceanography* **25**, PA2216 (2010).
176. Usdowski, E. & Hoefs, J. Oxygen isotope exchange between carbonic acid, bicarbonate, carbonate, and water: a re-examination of the data of McCrea (1950) and an expression for the overall partitioning of oxygen isotopes between the carbonate species and water. *Geochim. Cosmochim. Acta* **57**, 3815–3818 (1993).
177. Via, R. K. & Thomas, D. J. Evolution of Atlantic thermohaline circulation: Early Oligocene onset of deep-water production in the North Atlantic. *Geology* **34**, 441–444 (2006).
178. Vickers, M. L. et al. Cold spells in the Nordic Seas during the early Eocene Greenhouse. *Nat. Commun.* **11**, 1–12 (2020).
179. Voigt, J., Hathorne, E. C., Frank, M., Vollstaedt, H. & Eisenhauer, A. Variability of carbonate diagenesis in equatorial Pacific sediments deduced from radiogenic and stable Sr isotopes. *Geochim. Cosmochim. Acta* **148**, 360–377 (2015).
180. Voigt, J., Hathorne, E. C., Frank, M. & Holbourn, A. Minimal influence of recrystallization on middle Miocene benthic foraminiferal stable isotope stratigraphy in the eastern equatorial Pacific. *Paleoceanography* **31**, 98–114 (2016).
181. Wallmann, K. The geological water cycle and the evolution of marine $\delta^{18}O$ values. *Geochim. Cosmochim. Acta* **65**, 2469–2485 (2001).

182. Watkins, J. M. & Hunt, J. D. A process-based model for non-equilibrium clumped isotope effects in carbonates. *Earth Planet. Sci. Lett.* **432**, 152–165 (2015).
183. Watkins, J. M. & Devriendt, L. S. A combined model for kinetic clumped isotope effects in the $CaCO_3$-DIC-$H_2O$ system. *Geochem. Geophys. Geosyst.* **23**, e2021GC010200 (2022).
184. Westerhold, T., Röhl, U., Donner, B. & Zachos, J. C. Global extent of early Eocene hyperthermal events: A new Pacific benthic foraminiferal isotope record from Shatsky Rise (ODP Site 1209). *Paleoceanogr. Paleoclimatol.* **33**, 626–642 (2018).
185. Westerhold, T. et al. An astronomically dated record of Earth's climate and its predictability over the last 66 million years. *Science* **369**, 1383–1387 (2020).
186. de Winter, N. J., Agterhuis, T. & Ziegler, M. Optimizing sampling strategies in high-resolution paleoclimate records. *Clim. Past* **17**, 1315–1340 (2021).
187. Yu, J. & Elderfield, H. Mg/Ca in the benthic foraminifera Cibicidoides wuellerstorfi and Cibicidoides mundulus: Temperature versus carbonate ion saturation. *Earth Planet. Sci. Lett.* **276**, 129–139 (2008).
188. Zachos, J. C., Breza, J. R. & Wise, S. W. Early Oligocene ice-sheet expansion on Antarctica: Stable isotope and sedimentological evidence from Kerguelen Plateau, southern Indian Ocean. *Geology* **20**, 569–573 (1992).
189. Zachos, J., Pagani, M., Sloan, L., Thomas, E. & Billups, K. Trends, rhythms, and aberrations in global climate 65 Ma to present. *Science* **292**, 686–693 (2001).
190. Zachos, J. C. et al. Early Cenozoic extreme climates: Walvis Ridge transect. *Proc. ODP Init. Rep.* **208**, 1–112 (2004).
191. Zachos, J. C. *et al*. Rapid acidification of the ocean during the Paleocene-Eocene thermal maximum. *Science* **308**, 1611–1615 (2005).
192. Zachos, J. C., Dickens, G. R. & Zeebe, R. E. An early Cenozoic perspective on greenhouse warming and carbon-cycle dynamics. *Nature* **451**, 279–283 (2008).
193. Zachos, J. C., McCarren, H., Murphy, B., Röhl, U. & Westerhold, T. Tempo and scale of late Paleocene and early Eocene carbon isotope cycles: Implications for the origin of hyperthermals. *Earth Planet. Sci. Lett.* **299**, 242–249 (2010).
194. Zeebe, R. E. An explanation of the effect of seawater carbonate concentration on foraminiferal oxygen isotopes. *Geochim. Cosmochim. Acta* **63**, 2001–2007 (1999).
195. Zeebe, R. E. Seawater pH and isotopic paleotemperatures of Cretaceous oceans. *Palaeogeogr. Palaeoclimatol. Palaeoecol.* **170**, 49–57 (2001).
196. Zhang, Y. et al. Early Eocene vigorous ocean overturning and its contribution to a warm Southern Ocean. *Clim. Past* **16**, 1263–1283 (2020).
197. Zhang, Y. et al. Early Eocene ocean meridional overturning circulation: The roles of atmospheric forcing and strait geometry. *Paleoceanogr. Paleoclimatol.* **37**, e2021PA004329 (2022).

198. Zhang, S., Ji, W., Chen, H., Kirstein, L. A. & Wu, F. Linking rapid eruption of the Linzizong volcanic rocks and Early Eocene Climatic Optimum (EECO): Constraints from the Pana Formation in the Linzhou and Pangduo basins, southern Tibet. *Lithos* **446**, 107159 (2023).
199. Zhu, J., Poulsen, C. J. & Tierney, J. E. Simulation of Eocene extreme warmth and high climate sensitivity through cloud feedbacks. *Sci. Adv.* **5**, eaax1874 (2019).

**Acknowledgements**

This research was performed under the program of the Netherlands Earth System Science Centre (NESSC), being financially supported by the Ministry of Education, Culture, and Science (OCW) of the Netherlands. M.Z. acknowledges additional funding from the Dutch Research Council (NWO), research grant 016.161.365. This study used samples and data provided by the International Ocean Discovery Program (IODP). We thank Arnold E. van Dijk and Desmond D. Eefting (Geolab of Utrecht University) for technical support in the lab.

**Author contributions**

T.A., M.Z., and L.J.L. designed the study. T.A., B.O., S.K., B.L.P.K., L.V., M.K., S.P., and A.R. generated and analysed the stable and clumped isotope data. All authors contributed to data interpretation. T.A. wrote the article with input from all authors.

**Competing interests**

The authors declare no competing interests.

**Correspondence** and requests for materials should be addressed to Tobias Agterhuis

## Supplementary Information

### Mass spectrometry and clumped isotope data processing

Samples were measured in 73 runs over a period of approximately two years. Each run typically contained a mix of 22 samples (sometimes including samples from other projects) and 24 carbonate standards and lasted ~30 hours. The individual replicate measurements for the samples were distributed randomly over different runs and long periods. This approach was chosen in order to prevent possible biases in the obtained data due to short-term and long-term changes in the mass spectrometer performance. The relative proportion of the measured standards ETH-1, ETH-2, and ETH-3 was approximately 1:1:5, respectively. Measuring more of a standard that has a temperature close to the sample target (ETH-3 in this case) significantly reduces the uncertainty in the $\Delta_{47}$ sample data (Kocken et al., 2019).

Glass vials with small samples and standards, weighed in between 70 and 90 µg, were first loaded in an automatic carousel of the *Thermo Fisher Scientific Kiel IV* device. After this, the carbonates were individually dissolved with nominally anhydrous phosphoric acid (103% $H_3PO_4$) at 70 °C (Schmid & Bernasconi, 2010). The generated $CO_2$ gas from this reaction was purified using several steps in the instrument. First, the sample gas was captured in a first cryogenic liquid nitrogen ($LN_2$) trap at −196 °C. Here, $CO_2$ was separated from water and non-condensable gases. Subsequently, the gas was passed through a Porapak-Q trap kept at −50 °C used to remove organic compounds, such as halo-, hydrocarbons and sulphides (Schmid et al., 2012). To prevent contamination, the Porapak was cleaned by heating it to 150 °C for 1.5 hours before starting a new run. After these steps, the sample gas entered a second liquid nitrogen trap for one more purification step.

Eventually, a near pure $CO_2$ gas was transferred into a *Thermo Fisher Scientific MAT 253 Plus* instrument for isotope analysis. The mass spectrometer is equipped with Faraday cups for m/z 44–49, representing the different isotopologues of $CO_2$ (Gosh et al., 2006; Eiler et al., 2007; Schmid & Bernasconi, 2010). The m/z 48 and 49 signals were used to trace the presence of contaminants, as natural $CO_2$ gas is characterized by very low amounts of these two masses (Ghosh et al., 2006; Eiler et al., 2007; Bernasconi et al., 2013). The sample gas was measured against a reference gas of known isotopic composition ($\delta^{13}C$ = −2.82‰; $\delta^{18}O$ = −4.67‰) in order to obtain the necessary accuracy of the measurements (Huntington et al., 2009; Müller et al., 2017). The samples were measured in micro-volume mode using the long-integration dual-inlet (LIDI) workflow (Hu et al., 2014; Müller et al., 2017). This method first measures all sample gas before starting with the reference gas, to minimize the waste of gas. Pressure baseline effects were corrected during every run preparation by performing background scans using the reference gas at varying acceleration voltages (9.38–9.54 kV) and five m/z 44 intensities (5, 10, 15, 20, and 25 V) (Bernasconi et al., 2013; He et al., 2012; Meckler et al., 2014).

Subsequently, the three carbonate standards ETH-1, ETH-2, and ETH-3 were used to convert the raw $\Delta_{47}$ data of the samples into absolute values, to correct for drift in $\delta^{13}C$ and $\delta^{18}O$, and to correct for scale compression/stretching in $\delta^{18}O$. First, the $\Delta_{47}$ values of the measured samples and (check)standards were corrected using the offset between the measured $\Delta_{47}$ values of the ETH-3 standards and their accepted $\Delta_{47}$ values (see values below in this section). Only the neighbouring ETH-3 standards around the samples were used for this correction to account for trends in the mass spectrometer performance during the run. Next, the offset-corrected measured raw $\Delta_{47}$ values were normalized into the absolute reference frame (Dennis et al., 2011). Empirical transfer functions (ETF) were established, which represent linear regressions between the measured raw $\Delta_{47}$ and the internationally accepted (true) $\Delta_{47}$ values of all the three ETH standards (ETH-1: $\Delta_{47}$ = 0.2052±0.0016‰ (1SE); ETH-2: $\Delta_{47}$ = 0.2085±0.0015‰ (1SE); ETH-3: $\Delta_{47}$ = 0.6132±0.0014‰ (1SE) (Bernasconi et al., 2021). These ETFs transfer the raw $\Delta_{47}$ values into the InterCarb-Carbon Dioxide Equilibrium Scale (I-CDES90°C), which enables inter-laboratory comparison (Dennis et al., 2011; Bernasconi et al., 2018, 2021). The ETFs were constructed based on the ETH standards contained within a moving window of 250 measurements before and 250 measurements after (total, including both standards and sample measurements) each measurement. In practice, this implied that approximately 180 ETH-3 and 35 ETH-1 and ETH-2 measurements were used to establish the linear regression of the ETF. Subsequently, the final $\Delta_{47}$ values (as I-CDES90°C) of the samples were determined using the slope and intercept of the regression lines. To determine final $\delta^{13}C$ and $\delta^{18}O$ values of the samples, the raw values were corrected using the offset between the measured and accepted values of all the measured ETH standards in the same run (ETH-1: $\delta^{13}C_{VPDB}$ = 2.02±0.03‰, $\delta^{18}O_{VPDB}$ = −2.19±0.04‰; ETH-2: $\delta^{13}C_{VPDB}$ = −10.17±0.06‰, $\delta^{18}O_{VPDB}$ = −18.69±0.11‰; ETH-3: $\delta^{13}C_{VPDB}$ = 1.71±0.02‰, $\delta^{18}O_{VPDB}$ = −1.78±0.06‰) (Bernasconi et al., 2018).

The check standards (IAEA-C2 and Merck) were treated like samples and their final $\Delta_{47}$ values were used to monitor the corrections applied to the isotope data and to trace the instrument performance. Furthermore, the long-term averages of the final $\Delta_{47}$ values of ETH-1 and ETH-2 were monitored to verify the accuracy of the pressure baseline correction. This correction should result in these standards having the same $\Delta_{47}$ values (Bernasconi et al., 2018).

Some sample and standard measurements were excluded from the dataset based on criteria. First, sample and standard measurements with internal $\Delta_{47}$ standard deviations of >0.150 were considered bad measurements. Second, any contamination originating from impurities in the samples (and standards) were closely monitored by using the so-called '49 parameter' (John & Bowen, 2016). Measurements with a 49 parameter of >0.200 were regarded significantly contaminated. Third, measurements with too low (<8 V) or too high initial intensities (>40 V), and/or too big a difference between sample and reference gas intensity (>3 V) were removed. Fourth, sample

measurements with individual $\delta^{13}C$ and $\delta^{18}O$ values that have a big offset from the average value of the bin (offset >2‰) were considered unreliable, as these might contain contamination.

**Supplementary Figures**

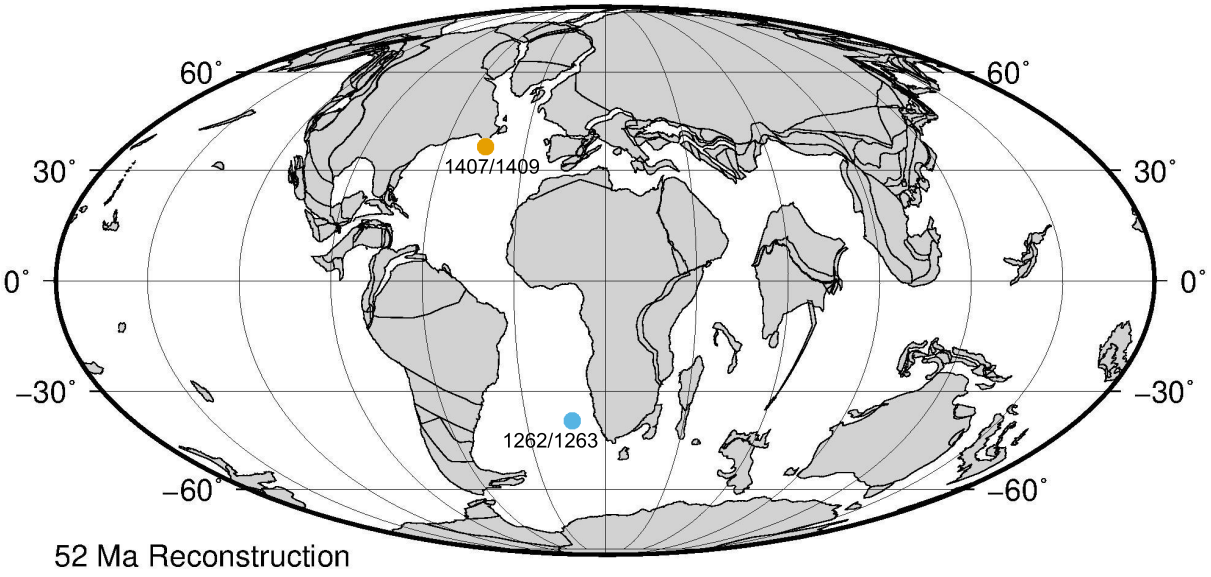


**Figure S1.** Paleogeographic reconstruction (52 Ma) with the locations of the South Atlantic (ODP Sites 1262 and 1263) and the North Atlantic (IODP Sites U1407 and U1409) sites. This map is generated from the plate tectonic reconstruction service of the Ocean Drilling Stratigraphic Network (ODSN; http://www.odsn.de).

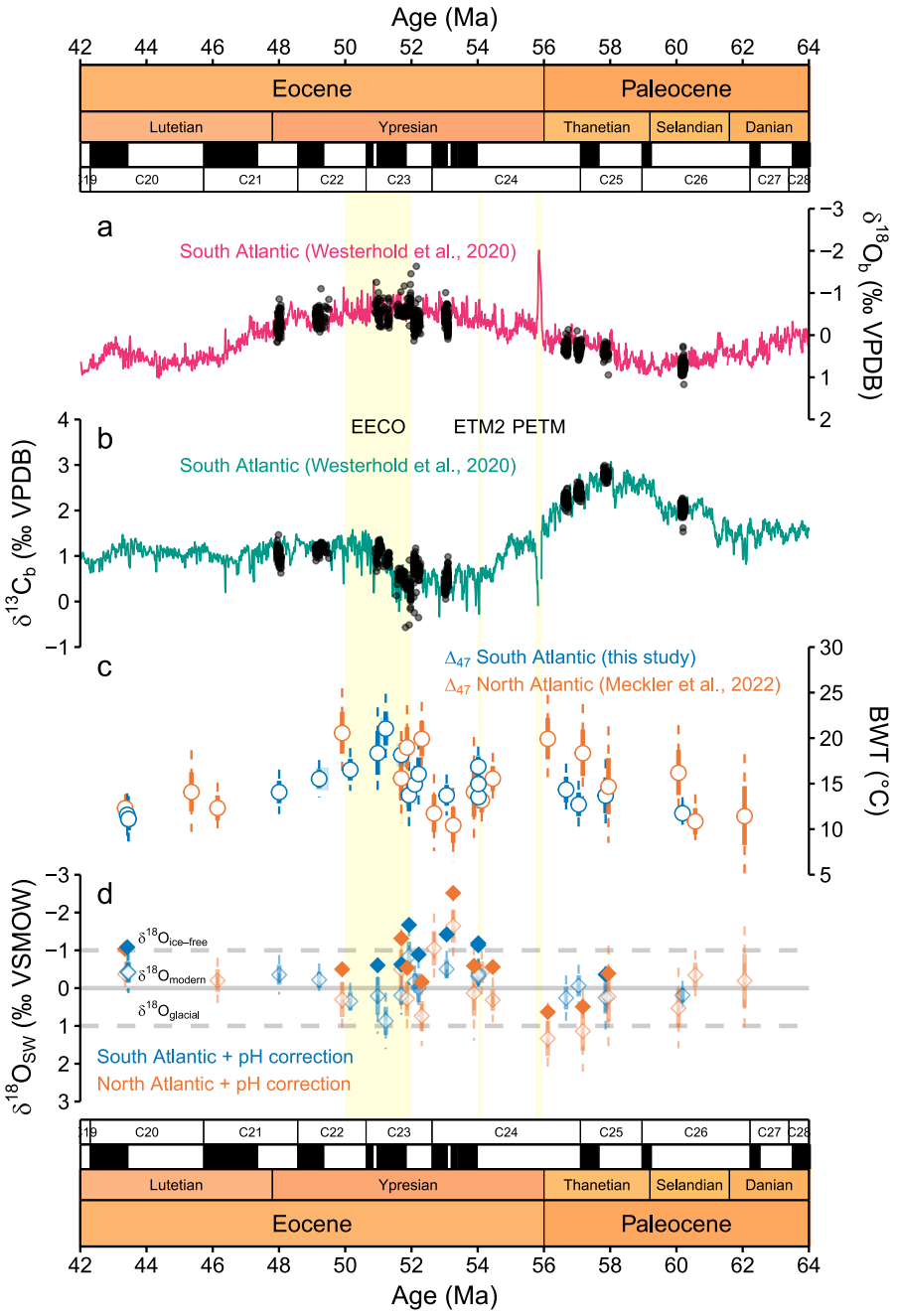


**Figure S2. a-b)** Comparison between our $\delta^{18}O_b$ and $\delta^{13}C_b$ measurements and published continuous high-resolution records of the Walvis Ridge, South Atlantic (ODP Sites 1262/1263/1265) (McCarren et al., 2008; Stap et al., 2010; Littler et al., 2014; Lauretano et al., 2015, 2016, 2018; Thomas et al., 2018; Barnet al., 2019; Westerhold et al., 2020). All $\delta^{18}O_b$ and $\delta^{13}C_b$ data are corrected towards *Cibicidoides* values, considered to represent seawater equilibrium (Marchitto et al., 2014). The high-resolution composite record shows relatively less scatter in the isotope values because it represents a 5 pts LOESS smoothing of data averaged in 5 kyr time steps. **c)** $\Delta_{47}$-based BWTs from the Walvis Ridge, South Atlantic (ODP Sites 1262/1263) (this study; Leutert et al., 2019; Agterhuis et al., 2022) and Newfoundland, North Atlantic (IODP Sites U1407/U1409) (Leutert et al., 2019; Meckler et al., 2022). **d)** inferred $\delta^{18}O_{sw}$ composition from the combined $\Delta_{47}$-based BWT and $\delta^{18}O_b$ data from the Walvis Ridge, South Atlantic (ODP Sites 1262/1263) (this study; Leutert et al., 2019; Agterhuis et al., 2022) and Newfoundland, North Atlantic (IODP Sites U1407/U1409) (Leutert et al., 2019; Meckler et al., 2022). The data represented with a closed fill indicate the $\delta^{18}O_{sw}$ values corrected for an assumed pH effect on the $\delta^{18}O_b$.

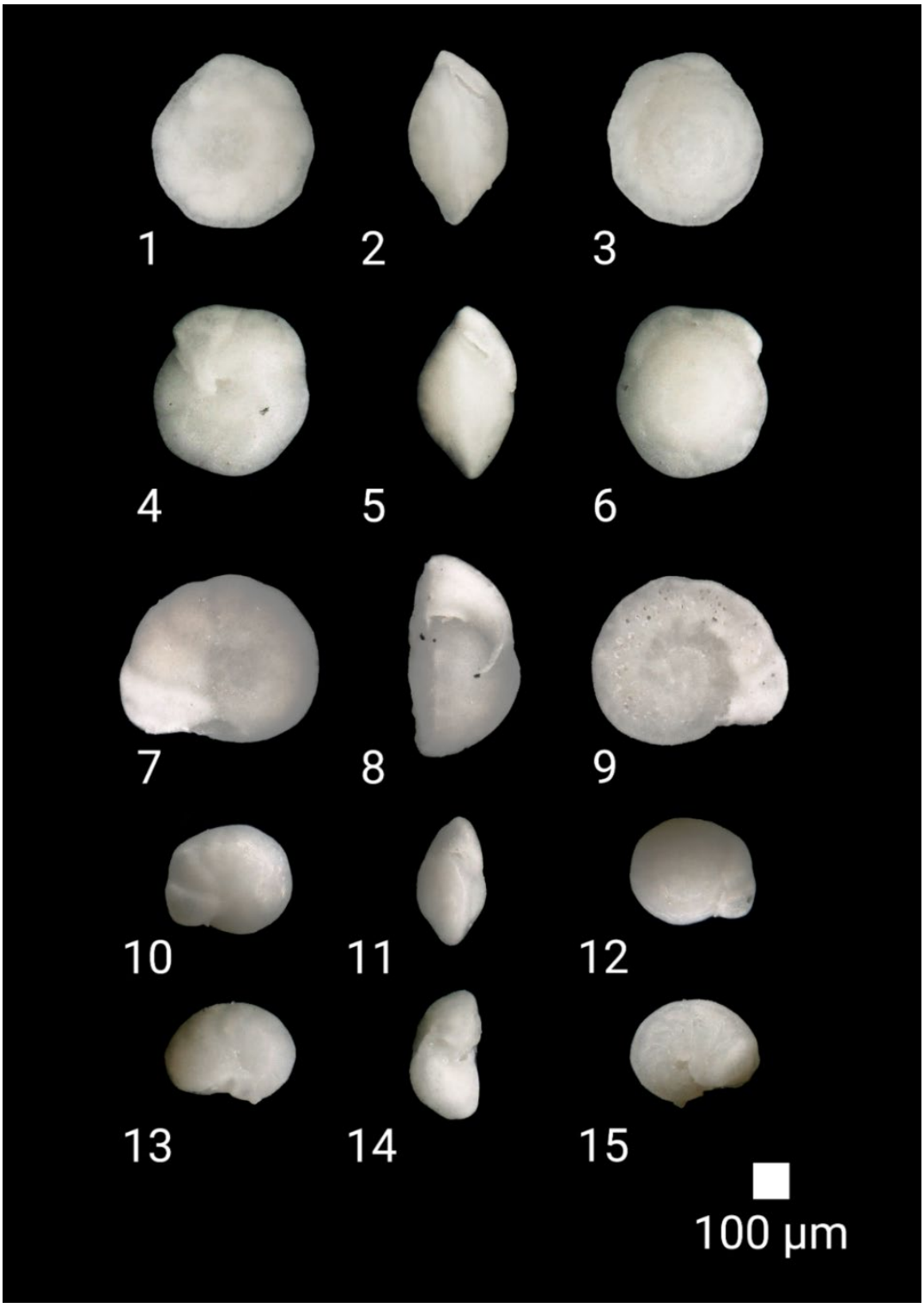


**Figure S3.** Images of benthic foraminiferal species measured for stable and clumped isotopes in this study. Pictures were taken using a Nikon Keyence VHX-5000 series digital microscope. Plates: (1) *Nuttallides truempyi* umbilical view, (2) apertural view, (3) spiral view (1263B 16H1W 84-85 cm); (4) *Oridorsalis umbonatus* umbilical view, (5) apertural view, (6) spiral view (1263B 16H1W 21-22 cm); (7) *Cibicidoides eocaenus* umbilical view, (8) apertural view, (9) spiral view (1263B 23H4W 54-55 cm); (10) *Cibicidoides mundulus* group umbilical view, (11) apertural view, (12) spiral view (1263B 23H4W 12-13 cm); (13) *Hanzawaia ammophila* umbilical view, (14) apertural view, (15) spiral view (1263B 23H4W 12-13 cm).

1031

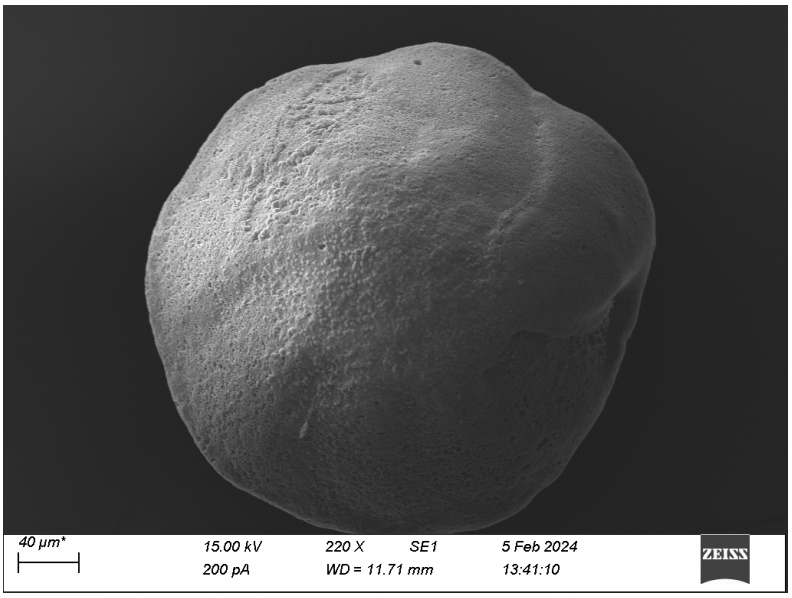


1032

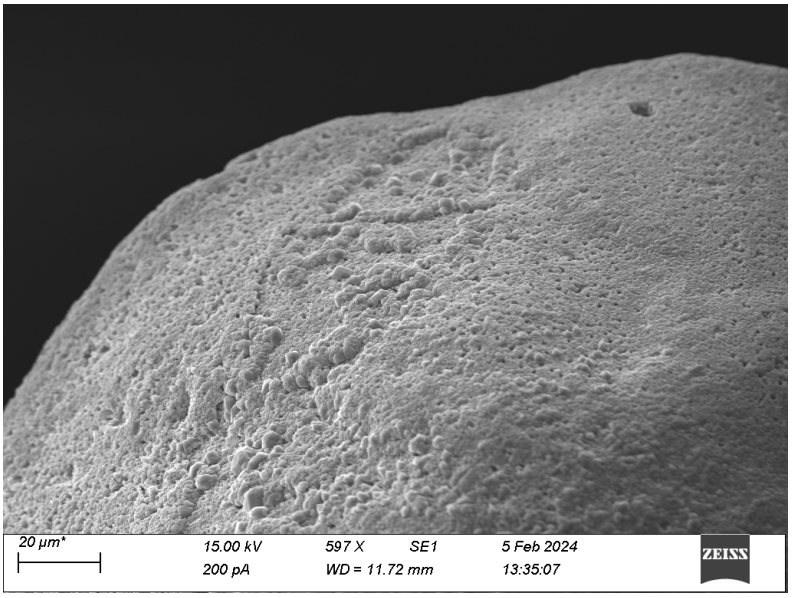


1033

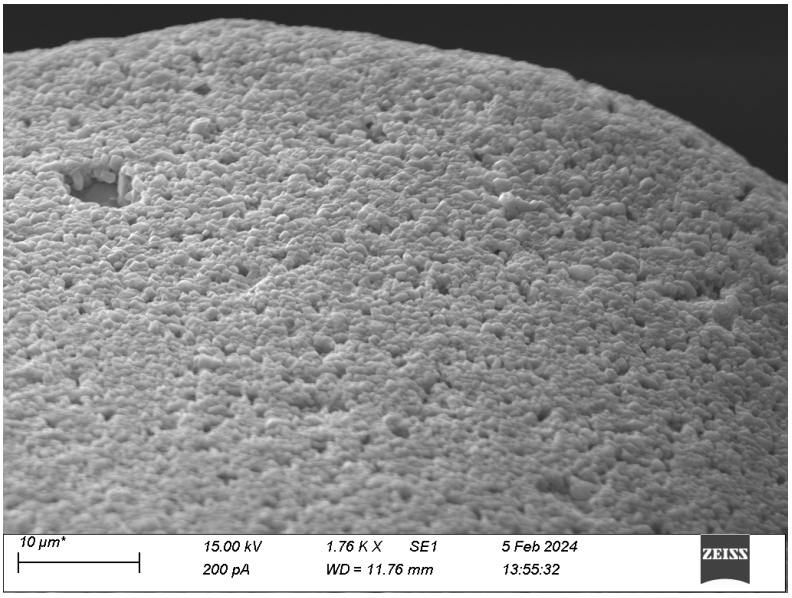

1034

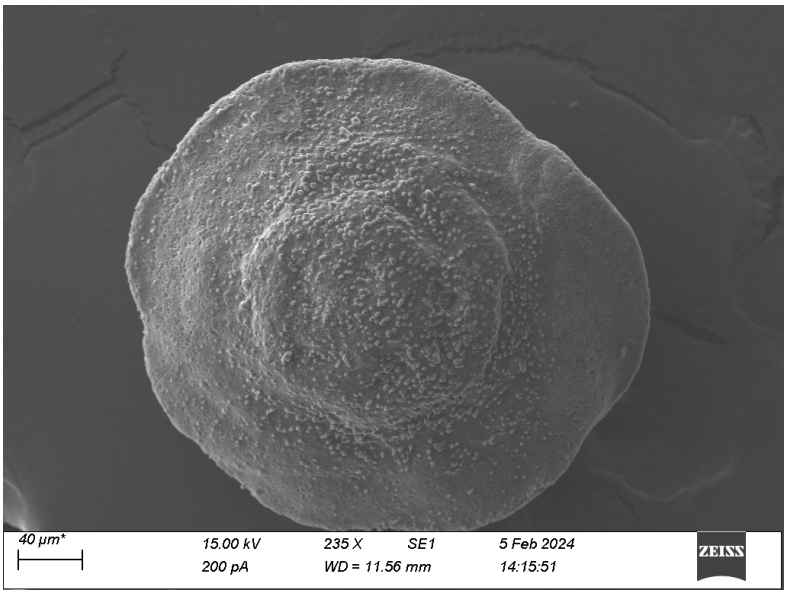


1035

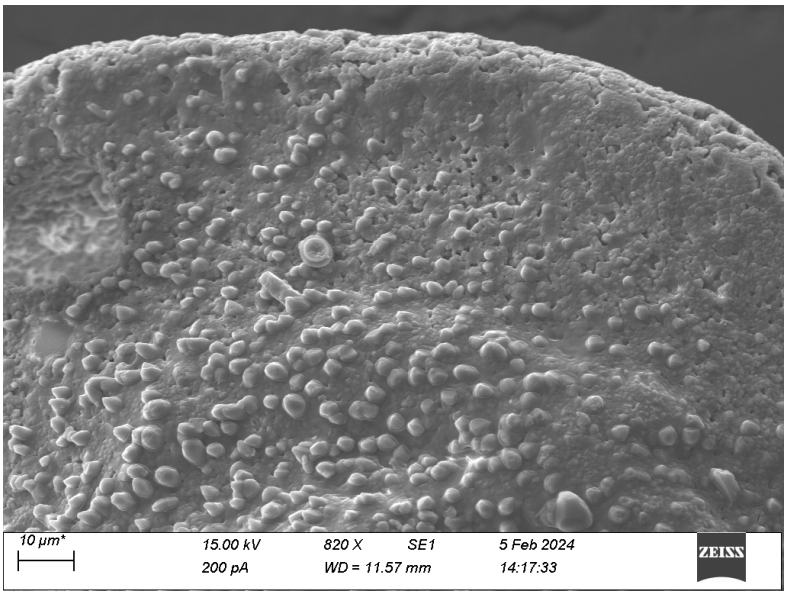


1036

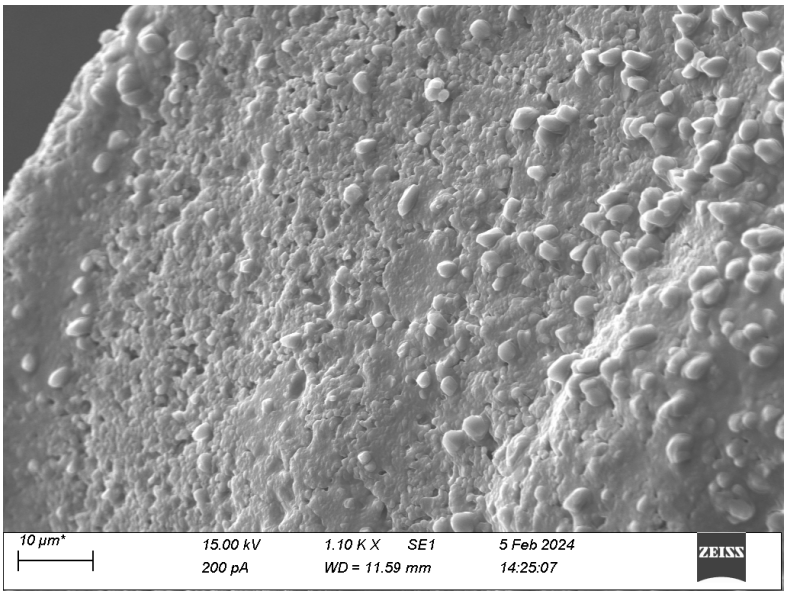

1037

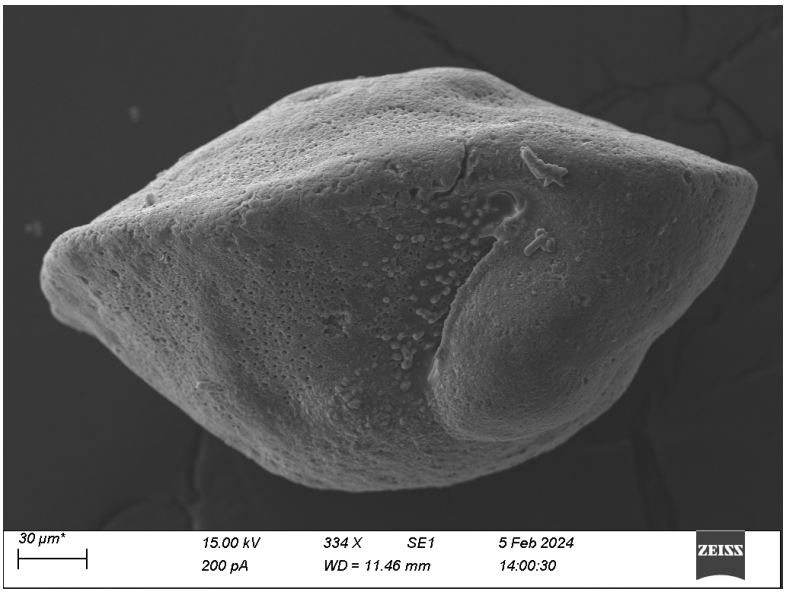


1038

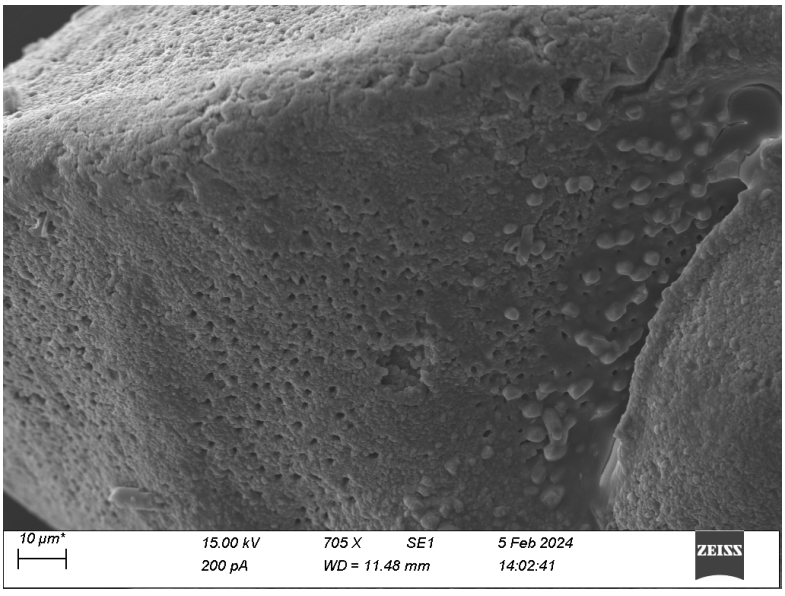


1039

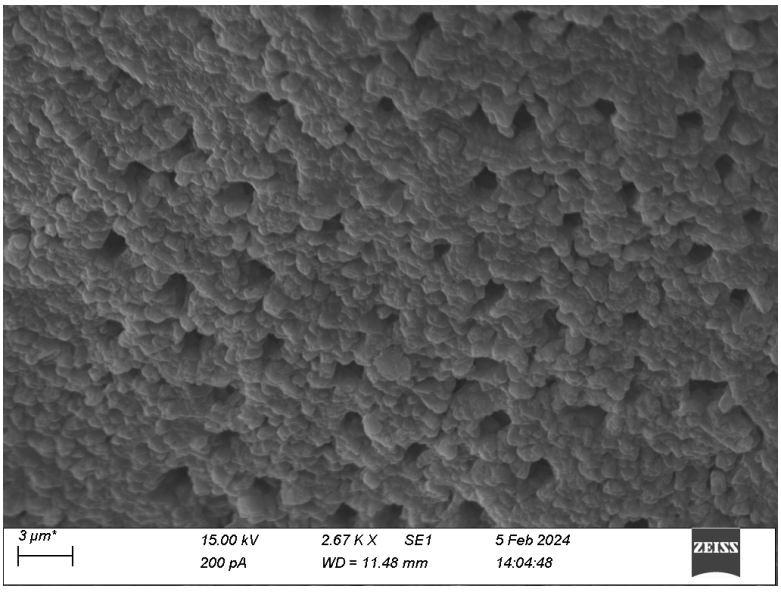

**Figure S4.** Scanning Electron Microscope (SEM) images of early Eocene *Nuttallides truempyi* specimens used in this study, from samples 1263B 20H3W 62-63 cm, 1263B 20H3W 79-80 cm, and 1263B 20H3W 94-95 cm (umbilical, spiral, and apertural view).

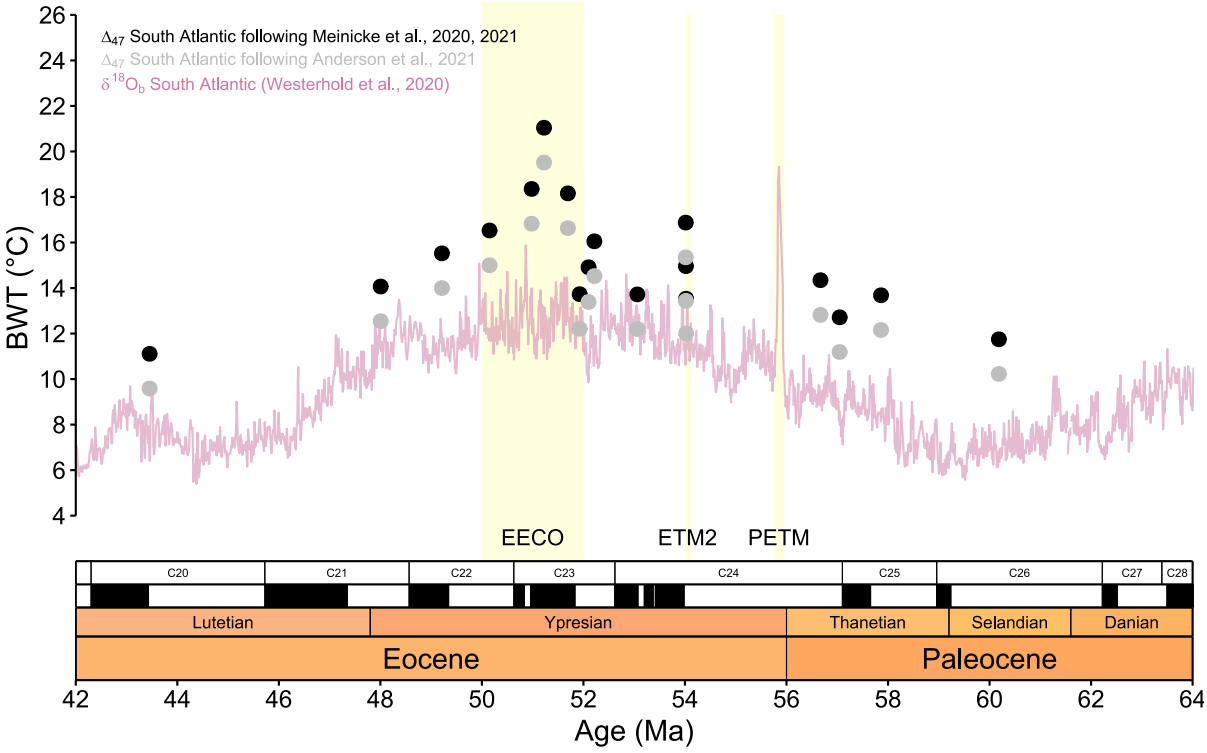


**Figure S5.** Comparison between $\Delta_{47}$-based BWTs of the South Atlantic (this study; Leutert et al., 2019; Agterhuis et al., 2022) following the foraminifer-based calibration by Meinicke et al., 2020, 2021 and the combined inorganic-biogenic calibration by Anderson et al., 2021. The $\delta^{18}O_b$ composite record consists of sites from the South Atlantic (Walvis Ridge) (McCarren et al., 2008; Stap et al., 2010; Littler et al., 2014; Lauretano et al., 2015, 2016, 2018; Thomas et al., 2018; Barnet al., 2019; Westerhold et al., 2020) and was corrected to *Cibicidoides* values (seawater equilibrium) before calculation of BWT using the calibration of Marchitto et al., 2014. The record represents a 5 pts LOESS smoothing of data averaged in 5 kyr time steps.

## Supplementary references


1. Agterhuis, T., Ziegler, M., de Winter, N. J. & Lourens, L. J. Warm deep-sea temperatures across Eocene Thermal Maximum 2 from clumped isotope thermometry. *Commun. Earth Environ.* **3**, 1–9 (2022).
2. Anderson, N. T. et al. A unified clumped isotope thermometer calibration (0.5–1,100 °C) using carbonate-based standardization. *Geophys. Res. Lett.* **48**, e2020GL092069 (2021).
3. Barnet, J. S. *et al*. A high-fidelity benthic stable isotope record of late Cretaceous–early Eocene climate change and carbon-cycling. *Paleoceanogr. Paleoclimatol.* **34**, 672–691 (2019).
4. Bernasconi, S. M. *et al*. Background effects on Faraday collectors in gas-source mass spectrometry and implications for clumped isotope measurements. *Rapid Commun. Mass Spectrom.* **27**, 603–612 (2013).
5. Bernasconi, S. M. et al. Reducing uncertainties in carbonate clumped isotope analysis through consistent carbonate-based standardization. *Geochem. Geophys. Geosyst.* **19**, 2895–2914 (2018).

6. Bernasconi, S. M. et al. InterCarb: A community effort to improve interlaboratory standardization of the carbonate clumped isotope thermometer using carbonate standards. *Geochem. Geophys. Geosyst.* **22**, e2020GC009588 (2021).
7. Dennis, K. J., Affek, H. P., Passey, B. H., Schrag, D. P. & Eiler, J. M. Defining an absolute reference frame for 'clumped' isotope studies of $CO_2$. *Geochim. Cosmochim. Acta* **75**, 7117–7131 (2011).
8. Eiler, J. M. "Clumped-isotope" geochemistry—The study of naturally-occurring, multiply-substituted isotopologues. *Earth Planet. Sci. Lett.* **262**, 309–327 (2007).
9. Ghosh, P. et al. $^{13}C$–$^{18}O$ bonds in carbonate minerals: A new kind of paleothermometer. *Geochim. Cosmochim. Acta* **70**, 1439–1456 (2006).
10. He, B., Olack, G. A. & Colman, A. S. Pressure baseline correction and high-precision $CO_2$ clumped-isotope ($\Delta_{47}$) measurements in bellows and micro-volume modes. *Rapid Commun. Mass Spectrom.* **26**, 2837–2853 (2012).
11. Hu, B. et al. A modified procedure for gas-source isotope ratio mass spectrometry: The long-integration dual-inlet (LIDI) methodology and implications for clumped isotope measurements. *Rapid Commun. Mass Spectrom.* **28**, 1413–1425 (2014).
12. Huntington, K. W. et al. Methods and limitations of 'clumped' $CO_2$ isotope ($\Delta_{47}$) analysis by gas-source isotope ratio mass spectrometry. *J. Mass Spectrom.* **44**, 1318–1329 (2009).
13. John, C. M. & Bowen, D. Community software for challenging isotope analysis: First applications of 'Easotope' to clumped isotopes. *Rapid Commun. Mass Spectrom.* **30**, 2285–2300 (2016).
14. Kocken, I. J., Müller, I. A. & Ziegler, M. Optimizing the use of carbonate standards to minimize uncertainties in clumped isotope data. *Geochem. Geophys. Geosyst.* **20**, 5565–5577 (2019).
15. Lauretano, V., Littler, K., Polling, M., Zachos, J. C. & Lourens, L. J. Frequency, magnitude and character of hyperthermal events at the onset of the Early Eocene Climatic Optimum. *Clim. Past* **11**, 1313–1324 (2015).
16. Lauretano, V., Hilgen, F. J., Zachos, J. C. & Lourens, L. J. Astronomically tuned age model for the early Eocene carbon isotope events: A new high-resolution $\delta^{13}C_{benthic}$ record of ODP Site 1263 between ~49 and ~54 Ma. *Newsl. Stratigr.* **49**, 383–400 (2016).
17. Lauretano, V., Zachos, J. C. & Lourens, L. J. Orbitally paced carbon and deep-sea temperature changes at the peak of the Early Eocene Climatic Optimum. *Paleoceanogr. Paleoclimatol.* **33**, 1050–1065 (2018).
18. Leutert, T. J. et al. Sensitivity of clumped isotope temperatures in fossil benthic and planktic foraminifera to diagenetic alteration. *Geochim. Cosmochim. Acta* **257**, 354–372 (2019).
19. Littler, K., Röhl, U., Westerhold, T. & Zachos, J. C. A high-resolution benthic stable-isotope record for the South Atlantic: Implications for orbital-scale changes in Late Paleocene–Early Eocene climate and carbon cycling. *Earth Planet. Sci. Lett.* **401**, 18–30 (2014).

20. Marchitto, T. M. et al. Improved oxygen isotope temperature calibrations for cosmopolitan benthic foraminifera. *Geochim. Cosmochim. Acta* **130**, 1–11 (2014).
21. McCarren, H., Thomas, E., Hasegawa, T., Röhl, U. & Zachos, J. C. Depth dependency of the Paleocene-Eocene carbon isotope excursion: Paired benthic and terrestrial biomarker records (Ocean Drilling Program Leg 208, Walvis Ridge). *Geochem. Geophys. Geosyst.* **9** (2008).
22. Meckler, A. N., Ziegler, M., Millán, M. I., Breitenbach, S. F. & Bernasconi, S. M. Long-term performance of the Kiel carbonate device with a new correction scheme for clumped isotope measurements. *Rapid Commun. Mass Spectrom.* **28**, 1705–1715 (2014).
23. Meckler, A. N. et al. Cenozoic evolution of deep ocean temperature from clumped isotope thermometry. *Science* **377**, 86–90 (2022).
24. Meinicke, N. et al. A robust calibration of the clumped isotopes to temperature relationship for foraminifers. *Geochim. Cosmochim. Acta* **270**, 160–183 (2020).
25. Meinicke, N., Reimi, M. A., Ravelo, A. C. & Meckler, A. N. Coupled Mg/Ca and clumped isotope measurements indicate lack of substantial mixed layer cooling in the Western Pacific Warm Pool during the last ~5 million years. *Paleoceanogr. Paleoclimatol.* **36**, e2020PA004115 (2021).
26. Müller, I. A. et al. Carbonate clumped isotope analyses with the long-integration dual-inlet (LIDI) workflow: Scratching at the lower sample weight boundaries. *Rapid Commun. Mass Spectrom.* **31**, 1057–1066 (2017).
27. Schmid, T. W. & Bernasconi, S. M. An automated method for 'clumped-isotope' measurements on small carbonate samples. *Rapid Commun. Mass Spectrom.* **24**, 1955–1963 (2010).
28. Schmid, T. W., Radke, J. & Bernasconi, S. M. Clumped-isotope measurements on small carbonate samples with a Kiel IV carbonate device and a MAT 253 mass spectrometer. *Appl. Note* **30233**, (Thermo Fisher, 2012).
29. Stap, L. *et al*. High-resolution deep-sea carbon and oxygen isotope records of Eocene Thermal Maximum 2 and H2. *Geology* **38**, 607–610 (2010).
30. Thomas, E. *et al*. Early Eocene thermal maximum 3: Biotic response at Walvis ridge (SE Atlantic ocean). *Paleoceanogr. Paleoclimatol.* **33**, 862–883 (2018).
31. Westerhold, T. et al. An astronomically dated record of Earth's climate and its predictability over the last 66 million years. *Science* **369**, 1383–1387 (2020).